Title

Optimization-Based Risk-Averse Outlier Accommodation With Linear Performance Constraints: Real-Time Computation and Constraint Feasibility in CAV State Estimation

Author

Hu, Wang

Publication Date

2024

UNIVERSITY OF CALIFORNIA
RIVERSIDE

Optimization-Based Risk-Averse Outlier Accommodation With Linear Performance Constraints: Real-Time Computation and Constraint Feasibility in CAV State Estimation

A Dissertation submitted in partial satisfaction
of the requirements for the degree of

Doctor of Philosophy

in

Electrical Engineering

by

Wang Hu

March 2024

Dissertation Committee:

Dr. Jay A. Farrell, Chairperson
Dr. Hamed Mohsenian-Rad
Dr. Guoyuan Wu

The Dissertation of Wang Hu is approved:

Committee Chairperson

University of California, Riverside

Acknowledgments

With heartfelt appreciation, I extend my deepest thanks to everyone who supported and contributed to the success of my research and the completion of my PhD dissertation.

First and foremost, I would like to express my profound gratitude to my advisor, Dr. Jay A. Farrell. His support, teachings, and encouragement have been the bedrock of my PhD journey. His patience, rigorous academic standards, and meticulous guidance have been instrumental in shaping me into a mature engineer. His warm smile and gentle demeanor have been a constant source of motivation, uplifting my spirits throughout the demanding path of my PhD.

I also wish to express my thanks to other members of my final defense committee, Dr. Hamed Mohsenian-Rad and Dr. Guoyuan Wu, for their invaluable advice and support in improving my dissertation. Collaborating with them on my projects and research has been both a pleasure and a privilege.

Additionally, I am grateful to my colleagues Dr. Farzana Rahman, Dr. Mohammad Billah, Dr. Felipe O. Silva, Dr. Elahe Aghapour, Dr. Zeyi Jiang, Jean-Bernard Uwineza, Xiaojun Dong, Ashim Neupane, Mike Stas, and Kathryn Hammar, for their collaboration in project development and research. I also want to thank Dr. Mohammed Khider and Dr. Guoyu Fu, my technical mentors during my internship at Google. Their professionalism and mentorship greatly expanded my technical knowledge and enhanced my communication skills, contributing to a harmonious work environment. Furthermore, I am thankful for my friends Jiaqing Chen, Zikui Cai, Xi Ding, Jie Xu, Xuangpeng Zhao, and Houjian Yu, for their friendship and the memorable times shared over the past five years.

Last but not least, my special thanks to my parents, Zhaoyang Hu and Qingquan Wang, for their endless love and unconditional support. The debt I owe them is immeasurable. Their resilience and steadfast love have been the guiding lights on my life's path.

To my loving parents,

your selfless love and support are the light that guides me,

always keeping me shining.

ABSTRACT OF THE DISSERTATION

Optimization-Based Risk-Averse Outlier Accommodation With Linear Performance Constraints: Real-Time Computation and Constraint Feasibility in CAV State Estimation

by

Wang Hu

Doctor of Philosophy, Graduate Program in Electrical Engineering
University of California, Riverside, March 2024
Dr. Jay A. Farrell, Chairperson

Connected and Autonomous Vehicles (CAV) require positioning that is consistently reliable and accurate. This is achieved through the choice of sensors and the real-time selection of high-quality measurements. Global Navigation Satellite Systems (GNSS) are the foundation to achieve accurate absolute positioning. GNSS Common-mode Errors (CME) mitigation can be realized with Differential GNSS (DGNSS) approach and Precise Point Positioning (PPP) techniques. With the evolution of International GNSS Service (IGS) Multi-GNSS Experiment (MGEX), Real-time PPP (RT-PPP) corrections for multi-GNSS have only recently become accessible.

GNSS measurements are prone to outliers. This results in an inherent performance versus risk trade-off in CAV state estimation applications. Recently proposed Risk-Averse Performance-Specified (RAPS) methods address this trade-off by optimally selecting a subset of measurements to minimize risk while achieving a target performance. The existing RAPS literature presents cases where the performance specification is stated for the full information matrix. However, those methods are not computationally efficient as required for real-time and do not address situations where that specification is infeasible.

This dissertation focuses on the Diagonal RAPS (DiagRAPS) formulation. This dissertation begins with a review of GNSS measurement models and real-time CME mitigation techniques, such as DGNSS, PPP, and Virtual Network DGNSS (VN-DGNSS). It then develops the theory of DiagRAPS for both binary and non-binary measurement selection variables. Algorithms suitable for real-time applications are proposed within Linear Programming (LP) and Mixed-Integer Linear Programming (ILP) optimization frameworks, achieving polynomial time-complexity. The convergence and computation costs of these algorithms are discussed. For binary DiagRAPS, a novel convex reformulation is derived, leading to a globally optimal solution that can be solved using existing tools. Additionally, a soft constraint optimization approach is proposed for situations when the specified performance is unfeasible. Finally, this dissertation evaluates DiagRAPS state estimation approaches using real-world multi-GNSS data from challenging environments for both DGNSS and RT-PPP applications. The results reveal that the locally optimal approach achieves state estimation performance comparable to the global solution. Both binary and non-binary DiagRAPS outperform traditional methods. Notably, the non-binary approach yielded the lowest computation cost and the best overall performance.

Contents

List of Figures

List of Tables

Acronyms

APC Antenna Phase Centre

BCD Block Coordinate Descent

BNC BKG NTRIP Client

CAS Chinese Academy of Sciences

CAV Connected and Autonomous Vehicles

CDMA Code Division Multiple Access

CME Common-mode Errors

CNES Centre national d'études spatiales

COM Center of Mass

DCB Differential Code Bias

DGNSS Differential GNSS

DiagRAPS Diagonal RAPS

DLR German Aerospace Center

ECEF Earth-Centered Earth-Fixed

FDMA Frequency Dvision Multiple Access

GNSS Global Navigation Satellite Systems

ICD Interface Control Document

IGS International GNSS Service

ILP Integer Linear Programming

IMU Inertial Measurement Unit

IOD Issue Of Data

IPP Ionosphere Pierce Point

ITS Intelligent Transportation System

KF Kalman Filter

LOS line-of-sight

LP Linear Programming

MAP Maximum A Posteriori

MGEX Multi-GNSS Experiment

NED North, East and Down

NOAA National Oceanic and Atmospheric Administration

OS Open Service

OSB Observable-specific Code Biases

OSR Observation Space Representation

PDF Probability Density Function

PPP Precise Point Positioning

PSD Power Spectral Density

PVA position, velocity, acceleration

RAPS Risk-Averse Performance-Specified

RMS Root Mean Square

RT-PPP Real-time PPP

RTCM Radio Technical Commission for Maritime Services

RTK Real-time Kinematic Positioning

SAE Society of Automotive Engineers

SF Single Frequency

SH Spherical Harmonic

SNR Signal-to-Noise Ratio

SSR State Space Representation

STD Standard Deviation

STEC Slant Total Electron Content

TD Threshold Decisions

TEC Total Electron Content

TECU TEC Units

TEX-CUP University of Texas Challenge for Urban Positioning

TGD Timing Goup Delay

UCR University of California-Riverside

US-TEC US Total Electron Content

VN-DGNSS Virtual Network DGNSS

VRS Virtual Reference Station

VTEC Vertical Total Electron Content

WHU Wuhan University

ZTD Zenith Troposphere Delay

Chapter 1

Introduction

1.1 Introduction

Within the framework of Intelligent Transportation System (ITS) and CAVs, reliable and accurate state estimation for localization is essential [1–3]. Accurate localization relies on sensor measurements from GNSS, vision, LIDAR, etc. Outliers commonly occur and can compromise these measurements. Outlier measurements are those that are very unlikely given the measurement model. A trade-off between performance and risk is inherent. In an ideal scenario where all measurements are outlier-free, utilizing all available data within a *maximum a posteriori* framework would lead to optimal state estimation accuracy. However, in practical scenarios, some measurements might be outliers (i.e, measurements that are extremely unlikely given the measurement model [4]). Therefore, each measurement offers the potential to provide enhanced estimation accuracy as quantified by the state error covariance matrix, provided it is outlier-free; however, each measurement that is added increases the risk that outlier measurements will corrupt the state estimate while causing the estimator to be overly confident in that corrupted estimate (i.e., the error covariance matrix is too small).

Precise and dependable localization and positioning are fundamental requirements for CAV applications [1]. Typically, accurate absolute positioning is facilitated by GNSS. For CAV applications, the Society of Automotive Engineers (SAE) J2945 specification defines the requirement for horizontal and vertical position errors to be less than 1.5 m and 3.0 m, respectively, with a probability of 68% [5]. However, standalone GNSS receivers, when not supplemented with external corrections, usually achieve positioning accuracy around 10 meters [6, 7]. This limitation is caused by CME in GNSS measurements, which can be attributed to factors such as inaccuracy in the broadcast satellite orbits and clocks, satellite hardware biases, and ionospheric and tropospheric delays [8]. CME are correlated over local areas (i.e., approximately $40km$).

Early and traditional methods to counteract the effects of CME employed Observation Space Representation (OSR) corrections. This approach is commonly associated with DGNSS, where receivers acquire lumped CME corrections either from a processing center or nearby base stations. DGNSS using pseudorange measurements typically yields an accuracy within the range of 0-3 meters. In contrast, DGNSS using phase measurements (often referred to as Real-time Kinematic Positioning (RTK)) can attain centimeter-level accuracy when integer ambiguities are correctly resolved [9]. However, these DGNSS advantages necessitate extensive local infrastructure and do not inherently provide corrections with global coverage.

The PPP technique is more appropriate for applications such as CAV that require global coverage. PPP uses State Space Representation (SSR), which utilizes models for each individual components of the CME [10]. Originally developed for post-processing in GPS surveying applications, PPP has recently advanced to the point where it is suitable for real-time GNSS operations [10, 11]. The IGS collaborates with global GNSS agencies, including Centre national d'études spatiales (CNES), Wuhan University (WHU), Chinese Academy of Sciences (CAS), German Aerospace Center (DLR), and others, to compute and supply globally relevant RT-PPP corrections with a low latency (approximately 10 seconds). This innovation enables users to receive CME corrections without the need for a nearby physical base station. With the continued progress of the IGS MGEX project, RT-PPP products for multi-GNSS systems (e.g., GPS, Galileo, BeiDou) have become accessible from some GNSS agencies.

With the rapid decline in the cost and size of sensors, the number of measurements available can far exceed the number that is required for observability of the state or for achieving a given accuracy specification. For example, state estimation using GNSS, the primary source for absolute position determination [12], requires pseudorange measurements from only four spatially diverse satellites per epoch [13]. Each GNSS satellite system generally provides 6-12 satellite observations per signal per epoch. Currently, four fully operational satellite constellations (i.e., BeiDou, GPS, Galileo, GLONASS) are available. Each has at least 2 ranging signals. This allows a receiver to receive at least 48-96 satellite ranging signals per epoch under open-sky conditions.

Such signal-rich environments offer new opportunities to optimize the selection of the least risky signals to use at each epoch to achieve a given performance specification. However, in challenging urban scenarios, such as areas with narrow streets flanked by tall buildings and trees, some GNSS signals may be obstructed or suffer from anomalies like multipath and non-line-of-sight effects [14]. These effects lead to a reduction in the number of available signals and an increased likelihood of outliers in the measurements that are actually received.

The performance versus risk trade-off and methodologies to optimize it are of paramount importance. In scenarios where a sufficient number of measurements m are utilized, adding one additional valid measurement only decreases the estimation error marginally (i.e., covariance decreases approximately as $\frac{1}{m}$); However, incorporating a single outlier-affected measurement can critically undermine the entire estimation process. This is because it not only corrupts the mean of the state estimate but also decreases the covariance, compromising the integrity of all subsequent outlier decisions.

State estimation using discrete-time measurements involves two steps. The time update propagates the posterior state estimate from the previous measurement epoch across the time span between measurements, to provide a prior state estimate at the next measurement epoch. The measurement update incorporates the measurement information to correct the prior state estimate to produce a posterior state estimate at the measurement time. Because outliers only affect the measurement update, this paper focuses entirely on the problem of measurement selection for the measurement update.

1.2 Outlier Accommodation Literature

The accommodation of outliers in state estimation is a well-studied problem. Standard methods for state estimation and control (see e.g.: [15–18]) evaluate measurement residuals against their expected values using a fixed or an adaptive threshold test, as will be reviewed in Section 5.1. More advanced approaches, such as Least Squares-based linear model fitting [19–21], least soft-threshold squares [22], least trimmed squares [23], and median least squares [24], have been developed for lease squares applications. These methods generally focus on detecting and either ignoring or de-weighting outliers, but do not address the risk-versus-performance trade-off involved with all measurements.

Recent advancements in outlier accommodation within an optimization framework have been developed [25–27]. N. Sünderhauf and P. Protzel [25] introduced latent variables to activate or deactivate measurements to achieve robust pose graph optimization. L. Carlone et al. [27] selected the maximal coherent subset of measurements for the same optimization problem. J. Shi et al. [26] proposed an approach to check the outliers in a subset of measurements through a compatibility test.

An alternative approach, RAPS state estimation, has been explored in [28, 29]. This estimation approach solves an optimal measurement selection and state estimation problem that tries to achieve a specified level of accuracy while incurring minimum risk. Previous RAPS studies formulated the optimization framework by using the full information matrix in the performance specification constraint, resulting in a semi-definite programming problem. The experimental evaluations of [28] were conducted under relative clear view of sky condition. The experimental evaluations of [29] focused on open-sky environments with artificially imposed outlier conditions. In both [28] and [29] the performance constraints were consistently feasible throughout the experiments; therefore, methods to address infeasibility were not discussed. Their data was from GPS-only so the number of available measurements m was not large. Additionally, these studies did not offer a computationally efficient method for solving the RAPS optimization problem, particularly for binary measurement selection variables. They relied on exhaustively evaluating all 2^m possible measurement combinations. Exhaustive evaluation has permutation time complexity which becomes computationally impractical as m increases. Although an approach incorporating only the diagonal elements of the information matrix into the performance specification constraint was mentioned, that problem and its computation efficient solution have not yet been investigated.

1.3 Contribution

This dissertation presents and demonstrates a computationally efficient solution to the RAPS problem with a diagonal performance specification (DiagRAPS) in the context of linear state estimation. Locally optimal approaches for both binary and non-binary measurement selection variables using the Block Coordinate Descent (BCD) method are proposed. The convergence and computation costs of the algorithm are discussed. A convex programming problem for the binary case is derived and formulated, leading to a globally optimal solution. It is significantly more efficient than the previously proposed methods that have permutation time complexity. These solutions are framed within the contexts of LP and Mixed-ILP problems. The experimental evaluation conducted multi-GNSS Single Frequency (SF) applications using both DGNSS and PPP approaches. For DGNSS, real-world driving data from hard urban environments was used, while for PPP, the data was collected under relatively clear sky conditions. These scenarios include numerous instances where the performance specification is infeasible (i.e., the constraint cannot be satisfied even with all measurements enabled). To address such scenarios, a relaxed optimization solution employing soft constraints for the LP or Mixed-ILP problem is proposed and evaluated.

The article is organized as follows: Chapter 2 reviews the GNSS measurement models and errors. Chapter 3 describes the GNSS real-time correction techniques from DGNSS and PPP. Chapter 4 outlines the linear state estimation problem and reviews Maximum A Posteriori (MAP) for the measurement update step using selected measurements. Chapter 5 reviews the Threshold

Decisions (TD) and DiagRAPS approaches. Chapter 6 presents solutions to DiagRAPS optimization problems, discussing convergence, optimality, and computation costs. Chapter 7 describes the experiments data source and analyzes DiagRAPS performance in DGNSS and PPP applications. Finally, Chapter 8 concludes the article and discusses future research directions.

Chapter 2

GNSS Models and Errors

2.1 GNSS Code Measurement Model

The signals transmitted by GPS, Galileo and BeiDou are based on Code Division Multiple Access (CDMA). GLONASS is based on Frequency Dvision Multiple Access (FDMA). For constellations based on CDMA, the frequencies are identical for all satellites. The measurement models presented in this section and the construction of this article are based on CDMA. For constellations based on FDMA, the frequency is different for each satellite and therefore for each receiver channel; therefore, there are additional frequency dependent *inter-channel biases* (ICBs) terms in both code and carrier phase observation equations [30, 31]. This research focus on GNSS applications using CDMA and single frequency.

For each GNSS constellation γ, that uses CDMA, transmits signals using f carrier frequencies. The SF code (pseudorange) observation from satellite s tracked by receiver r at the GNSS

Table 2.1: Notation definitions.

c: Speed of light (m/s),

δ^s: Satellite clock model error, $\delta^s = (c\,\hat{dt}^s - \Delta^s)$, (m),

$\hat{dt}^s$: Broadcast satellite clock correction (s),

Δ^s: Satellite clock bias (m),

B^s_f: Satellite code hardware bias (m),

Δ^γ_r: Receiver clock bias for constellation γ (m),

T^s_r: Tropospheric delay (m),

$I^s_{f,r}$: Ionospheric delay for f frequency (m),

M^s_r: Multipath error (m),

$\eta^s_{r,\rho}$: Random code measurement noise (m).

receiver time t_r is modeled as (see Chap. 21 of [9])

$$\left.\begin{aligned} \rho^s_{f,r}(t_r) = & R\Big(\mathbf{p}_r(t_r), \hat{\mathbf{p}}_s(t_s)\Big) + \Delta^\gamma_r + M^s_r + \eta^s_{r,\rho} \\ & + E^s_r - \Delta^s + B^s_f + T^s_r + I^s_{r,f}, \end{aligned}\right\} \tag{2.1}$$

where $\mathbf{p}_r$ denotes the receiver antenna position, $\hat{\mathbf{p}}_s$ denotes the satellite position, while t_s denotes the time when the signal was transmitted. The terms $\mathbf{p}_r$ and $\hat{\mathbf{p}}_s$ will be further discussed in Sec. 2.3. E^s_r denotes the satellite range ephemeris error in meters which is modeled as

$$E^s_r = R\Big(\mathbf{p}_r(t_r), \mathbf{p}_s(t_s)\Big) - R\Big(\mathbf{p}_r(t_r), \hat{\mathbf{p}}_s(t_s)\Big)$$

where $\mathbf{p}_s$ represents the true satellite position. Other important symbols are defined as in Table 2.1. The measurement noise is assumed to be white and uncorrelated between satellites.

2.2 GNSS Code Measurement Errors

The goal of the state estimator using GNSS is to accurately estimate the state vector, which will include the position $\mathbf{p}_r$ and the receiver clock bias Δ_r^{γ}. The satellite clock bias Δ^s can be corrected by the broadcast satellite clock correction, denoted as $\hat{dt}^s$, using ephemeris. The model for $\hat{dt}^s$, which includes a polynomial and a relativistic correction, can be found in the Interface Control Document (ICD) of each constellation [32–34]. The remaining satellite clock model error is

$$\delta^s = (c\hat{dt}^s - \Delta^s). \tag{2.2}$$

The error terms of the measurement model of eqn. (2.1) can be classified into two categories:

- CME are essentially the same for all receivers in a local vicinity. They are grouped in the second line of eqn. (2.1). These include: satellite range ephemeris and clock model errors, satellite code hardware bias, and atmospheric (ionospheric and tropospheric) error.
- Non-CME are different for each receiver. These include: code multipath error and random code measurement noise.

These errors significantly affect the positioning accuracy. The typical error magnitudes are summarized in Table. 2.2. The CME mitigation techniques will be detailed in Chapter 3. The non-CME will be discussed in Sec. 4.3

Table 2.2: GNSS range measurement error magnitudes.

Error Source	Typical Magnitude	Reference
Satellite range ephemeris	~ 2 m	[35]
Satellite clock	~ 5 ns	[35]
Satellite code bias	~ 20 ns	[36–38]
Troposphere delay	~ 2.3 m	[39]
Ionosphere delay	< 30 m	Sec. 25.2 in [9]
Code multipath	< 3 m	Sec. 8.4.7 in [8]
Measurement noise	< 1 mm	Sec. 19.7.1 in [9]

2.3 Geometric Range Model and Linearization

Both $\mathbf{p}_r$ and $\hat{\mathbf{p}}_s$ are defined in the Earth-Centered Earth-Fixed (ECEF) frame. Because the ECEF frame is rotating, the range quantity in Eqn. (2.1) must be interpreted carefully, as the ECEF frame is oriented differently at times t_s and t_r. Let E_r and E_s represent the ECEF frames at time t_r and t_s respectively. The rotation matrix $\mathbf{R}_{E_s}^{E_r}$ rotates vectors from their representation in frame E_s to E_r (See eqn. (2) in [40]). Therefore, the geometric range term is expressed as

$$R(\mathbf{p}_r^{E_r}(t_r), \hat{\mathbf{p}}_s^{E_r}(t_s)) = \|\mathbf{p}_r^{E_r}(t_r) - \hat{\mathbf{p}}_s^{E_r}(t_s)\|,$$

where $\mathbf{p}_r^{E_r}(t_r) = \mathbf{p}_r(t_r)$, $\hat{\mathbf{p}}_s^{E_s}(t_s) = \hat{\mathbf{p}}_s(t_s)$, and $\hat{\mathbf{p}}_s^{E_r}(t_s) = \mathbf{R}_{E_s}^{E_r}\,\hat{\mathbf{p}}_s^{E_s}(t_s)$ where $\hat{\mathbf{p}}_s^{E_s}(t_s)$ represent the satellite position at t_s in E_s frame which can be calculated using ephemeris. The rotation matrix $\mathbf{R}_{E_s}^{E_r}$ is a function of signal's time-of-transmission t_T. Utilizing the pseudo time-of-transmission computed from code measurement could affect the accuracy of satellite position rotation, dominated by the receiver clock bias Δ_r^{γ}, particularly in the case of low-cost receivers [40].

Alternatively, this geometric range can be computed by the well-known Sagnac correction:

$$R(\mathbf{p}_r^{E_r}(t_r), \hat{\mathbf{p}}_s^{E_r}(t_s)) = \|\mathbf{p}_r^{E_r}(t_r) - \hat{\mathbf{p}}_s^{E_s}(t_s)\| + \frac{\boldsymbol{\omega}_e}{c}(\mathbf{p}_r^{E_r}(t_r) \times \hat{\mathbf{p}}_s^{E_s}(t_s)) \tag{2.3}$$

$$= \|\mathbf{p}_r^{E_r}(t_r) - \hat{\mathbf{p}}_s^{E_s}(t_s)\| + \frac{\omega_{ie}}{c}(xb - ay), \tag{2.4}$$

where $\boldsymbol{\omega}_e = [0, 0, \omega_{ie}]^\top$, ω_{ie} is the earth rotation rate, $\hat{\mathbf{p}}_s = [x, y, z]^T$, and $\mathbf{p}_r = [a, b, \kappa]^T$. Eqn. (2.4) offers a more computationally efficient implementation than eqn. (2.3) due to $\boldsymbol{\omega}_e$ containing two zero elements. The derivation of Sagnac correction can be found in [41]. The accuracy of the Sagnac correction is shown to be accurate to 7.34×10^{-4} m. In addition, $\hat{t}_T = R(\mathbf{p}_r^{E_r}(t_r), \hat{\mathbf{p}}_s^{E_r}(t_s))/c$ can be used to approximate the signal time-of-transmission for the computation of $\mathbf{R}_{E_s}^{E_r}$.

For the subsequent discussion, the time notation '(t_r)' and '(t_s)' are dropped. Given an initial rover position $\mathbf{p}_0$, the first-order Taylor series expansion of $R(\mathbf{p}_r, \hat{\mathbf{p}}_s)$ at $\mathbf{p}_r = \mathbf{p}_0$ yields

$$R(\mathbf{p}_r, \hat{\mathbf{p}}_s) \approx R(\mathbf{p}_0, \hat{\mathbf{p}}_s) + (\mathbf{1}_r^s)^\top(\mathbf{p}_r - \mathbf{p}_0) \tag{2.5}$$

where $\mathbf{1}_s^r$ is the line-of-sight (LOS) vector from the satellite to the receiver, defined as

$$\mathbf{1}_s^r = \frac{\mathbf{p}_0 - \hat{\mathbf{p}}_s}{\|\mathbf{p}_0 - \hat{\mathbf{p}}_s\|}. \tag{2.6}$$

The geometric range is typically on the order of 10^7 meters. If $\mathbf{p}_0$ is within 100 meters of the actual position, the magnitude of higher-order terms is less than one millimeter, which is smaller than the magnitude of the measurement noise, and therefore negligible. In GNSS applications, this $\mathbf{p}_0$ can be given by the predicted position from the prior state so that $\|\mathbf{p}_0 - \mathbf{p}_r\|$ is typically less than 100 meters.

2.4 GNSS Doppler Measurement Model

For satellite s, the Doppler measurement is modeled as

$$-\lambda_f D_s = (\mathbf{1}_s^r)^\top (\mathbf{v}_r - \mathbf{v}_s) + r_c - \dot{\Delta}^s + \eta_{r,D}^s \tag{2.7}$$

where λ_f is the wavelength of f frequency, $\mathbf{v}_r \in \Re^3$ denotes the rover velocity at t_r in E_r frame, r_c is the receiver clock drift in meters per seconds, $\mathbf{v}_s \in \Re^3$ denotes the satellite velocity at t_s in E_s frame where $\mathbf{v}_s = \mathbf{R}_{E_s}^{E_r} \mathbf{v}_s^{E_s}$, $\mathbf{v}_s^{E_s}$ and $\dot{\Delta}^s$ denotes the satellite velocity (m/s) in E_s frame and clock drift (m/s) which can be computed using ephemeris, and $\eta_D^s \sim \mathcal{N}(0, \sigma_{s,D})$ is the Doppler measurement noise which is assumed to be white and uncorrelated between satellites. Note that the receiver clock drift rate is identical for all constellations.

Chapter 3

GNSS Real-time Correction Techniques

In real-time applications, three methods to effectively improve the GNSS positioning accuracy are discussed herein. First, DGNSS approaches use OSR corrections. GNSS measurements from a receiver at a known location near to the user receiver are communicated to the user receiver, which forms differential measurements that are essentially free from common-mode errors [42]. Second, PPP approaches rely on correction information communicated in SSR format. The correction information for each portion of the common-mode range errors are separately communicated from an on-line data source to the receiver [36, 43]. Third, the recently developed VN-DGNSS constructs OSR corrections using RT-PPP techniques with global dissemination coverage. This approach requires the receiver's native solution (i.e., the correction is directly input into the receivers through the Radio Technical Commission for Maritime Services (RTCM) protocol) and eliminates the additional need for physical reference stations.

3.1 DGNSS

The fundamental constitution of DGNSS is reference stations that transmit corrections or observations that align with its accurately-surveyed position to users. If the corrections are determined by the data from a single reference station, it is known as local DGNSS. DGNSS is a widely-utilized and effective technique for mitigating the common-mode errors within a local vicinity (see Section 8.8 in [8]). This mitigation is accomplished through a single-difference operation between the rover's measurements and base station's corrections. The base station antenna and its location should be selected to minimize multipath effects.

In the code-based DGNSS, the code and Doppler measurement model for the base station at time t_b is similar to eqn. (2.1),

$$\rho^s_{f,b}(t_b) = R(\mathbf{p}_b, \hat{\mathbf{p}}_s) + \Delta^\gamma_b + E^s_b - \Delta^s + B^s_f + T^s_b + I^s_{b,f} + M^s_b + \eta^s_{b,\rho}. \tag{3.1}$$

The difference $t_r - t_b$ is indicated as communication latency of DGNSS, which demonstratively achieve 95% sub-meter accuracy probability with latency less than 600 seconds [42]. The base station position $\mathbf{p}_b$ is static and known to centimeter accuracy. Therefore, the differential correction is computed as

$$\begin{aligned} C_b &= \rho^s_{f,b}(t_b) - R(\mathbf{p}_b, \hat{\mathbf{p}}_s) \\ &= \Delta^\gamma_b + E^s_b - \Delta^s + B^s_f + T^s_b + I^s_{b,f} + M^s_b + \eta^s_\rho. \end{aligned} \tag{3.2}$$

The single-differenced code measurement model for satellite s is

$$\begin{aligned}\delta\rho^s_{OSR} &= \rho^s_{f,r}(t_r) - C_b \\ &= R(\mathbf{p}_r, \hat{\mathbf{p}}_s) + \Delta^{\gamma}_{r,OSR} + M^s_{r,OSR} + \varepsilon^s_{r,OSR},\end{aligned} \tag{3.3}$$

where $\Delta^{\gamma}_{r,OSR} = \Delta^{\gamma}_r - \Delta^{\gamma}_b$ represents the single-differenced receiver clock bias, $M^s_{r,OSR} = M^s_r - M^s_b$, and

$$\varepsilon^s_{r,OSR} = E^s_r - E^s_b + T^s_r - T^s_b + I^s_{r,f} - I^s_{b,f} + \eta^s_{r,\rho} - \eta^s_{b,\rho} \tag{3.4}$$

represents the residual of CME and measurement noise.

3.2 Real-time PPP

SSR correction service is the latest generation GNSS service, which is usually indicated to PPP. PPP was introduced since 1997 [44] but its under continuously developing. Unlike DGNSS, PPP does not require simultaneous observations from nearby base stations. PPP approach process undifferenced GNSS measurements with correcting each common-mode errors using empirical correction models or real-time correction service [11, 12].

3.2.1 Satellite Orbit and Clock Corrections

The SSR data streams provide orbit and clock products to correct the satellite position $\hat{\mathbf{p}}_s(t_s)$ and clock error $\delta^s(t_s)$ at the transmit time t^s.

The orbit correction consists of orbit $\delta\mathbf{O} = [\delta O_r, \delta O_a, \delta O_c]^T$ and rate $\delta\dot{\mathbf{O}} = [\delta\dot{O}_r, \delta\dot{O}_a, \delta\dot{O}_c]^T$ corrections along with a reference time t_o. These define radial (δO_r, $\delta\dot{O}_r$), along-track (δO_a, $\delta\dot{O}_a$) and cross-track (δO_c, $\delta\dot{O}_c$) components. The calculation has five steps [10,42]:

1. Compute the satellite orbit correction $\mathbf{O}$ for time t_s:

$$\mathbf{O}(t_s) = \delta\mathbf{O} - \delta\dot{\mathbf{O}} \cdot (t_s - t_o).$$

2. Compute the along-track $\mathbf{e}_a$, cross-track $\mathbf{e}_c$, and radial $\mathbf{e}_r$ direction unit vectors:

$$\mathbf{e}_a = \frac{\hat{\mathbf{v}}_s(t_s)}{|\hat{\mathbf{v}}_s(t_s)|}, \mathbf{e}_c = \frac{\hat{\mathbf{p}}_s(t_s) \times \hat{\mathbf{v}}_s(t_s)}{|\hat{\mathbf{p}}_s(t_s) \times \hat{\mathbf{v}}_s(t_s)|}, \mathbf{e}_r = \mathbf{e}_a \times \mathbf{e}_c,$$

where $\hat{\mathbf{v}}_s$ is the satellite velocity and × denotes the vector cross product.

3. Transform the corrections to the ECEF frame at t_s:

$$\delta\mathbf{p}_s(t_s) = [\mathbf{e}_r, \mathbf{e}_a, \mathbf{e}_c]\,\Delta\mathbf{O}(t_s).$$

4. Correct the broadcast position $\hat{\mathbf{p}}_s(t_s)$ to precise position $\tilde{\mathbf{p}}_s(t_s)$:

$$\tilde{\mathbf{p}}_s(t_s) = \hat{\mathbf{p}}_s(t_s) - \delta\mathbf{p}_s(t_s).$$

5. Compute satellite range ephemeris error $\hat{E}_r^s$:

$$\hat{E}_r^s = R(\mathbf{p}_r(t_r), \tilde{\mathbf{p}}_s(t_s)) - R(\mathbf{p}_r(t_r), \hat{\mathbf{p}}_s(t_s)).$$

The satellite clock correction is transmitted as three polynomial parameters (C_i^s, $i=0,1,2$) with a corresponding reference time t_c^s. The clock correction for satellite s at transmit time t^s is:

$$\delta C^s(t^s) = C_0^s + C_1^s(t^s - t_c^s) + C_2^s(t^s - t_c^s) \quad \text{meters.} \tag{3.5}$$

To be consistent with eqn. (4) in [45], the correction of satellite clock model error $\hat{\delta}^s$ (i.e., correction of the broadcast clock error) is

$$\hat{\delta}^s = -\delta C^s(t^s) \quad \text{seconds.} \tag{3.6}$$

3.2.2 Satellite Hardware Bias

Satellite hardware biases have various causes such as analog group delays in the front-end and digital delays. They are normally very stable over time (i.e., constant over at least a single day) [46]. GNSS OS users can apply the Timing Goup Delay (TGD) to roughly correct the hardware bias [47]. The TGD is computed by the GNSS control segment and broadcast in the navigation message for GNSS Open Service (OS) users.

To attain higher accuracy, SSR operations may use either Differential Code Bias (DCB) or Observable-specific Code Biases (OSB) corrections, as defined in the SINEX standard [48]. For the OSB product, let the symbol $B_{(\mathbf{S},T)}$ to denote the correction for observation type T of constellation **S** (e.g., T could be the C1C observation type with S denoting GPS). The $B_{(\mathbf{S},T)}$ correction products are available in SSR format from sources such as CAS GIPP [49]. For SSR users, the observation $O_{(\mathbf{S},T)}$ is corrected by $B_{(\mathbf{S},T)}$ as

$$O'_{(\mathbf{S},T)} = O_{(\mathbf{S},T)} - B_{(\mathbf{S},T)} \tag{3.7}$$

to produce the OSB-corrected observation $O^{'}_{(\mathbf{S},T)}$.

For the code measurement in eqn. (2.1),

$$\hat{B}^{s}_{f} = B_{(\mathbf{S},T)}. \tag{3.8}$$

3.2.3 Global Troposphere Model

The troposphere is the lowest layer of the atmosphere, extending to about 60 kilometers above the Earth's surface. In this layer, the speed of light is slower than in a vacuum, so the radio signal is delayed. The delay is affected by numerous meteorological parameters relevant within the vicinity of the receiver, e.g., temperature, pressure, and relative humidity. Numerous tropospheric delay correction models have been introduced [50–52]. These models avoid the need for real-time measurement of the meteorological parameters.

IGGtrop [51] is one such global empirical model. It computes the correction for the slant troposphere delay T^{s}_{r} as:

$$\hat{T}^{s}_{r}(E,t) = M(E)\ T_{z}(t) \tag{3.9}$$

where E is the satellite elevation angle at the rover position;

$$M(E) = 1.001\left(0.002001 + sin^{2}(E)\right)^{-\frac{1}{2}}$$

is the mapping function [53] for converting the Zenith Troposphere Delay (ZTD) to the slant tropospheric delay; and, $T_{z}(t)$ is the ZTD (i.e., tropospheric delay in the zenith direction above the receiver). IGGtrop computes $T_z(t)$ as

$$\begin{aligned} T_z(t) =& a_0 + a_1\, cos(\gamma\, t) + a_2\, sin(\gamma t) \\ & + a_3\, cos(2\,\gamma\, t) + a_4\, sin(2\,\gamma\, t) \end{aligned} \tag{3.10}$$

where $\gamma = (2\pi/365.25)$ and the units of t are real-valued days of the year. The coefficients a_0, (a_1, a_2) and (a_3, a_4) model the mean value, the annual variation and the semi-annual variation in ZTD, respectively. IGGtrop defines these parameters on a 3-D grid in latitude, longitude, and altitude around the globe. This enables interpolation of the ZTD at a receiver position to achieve 3.86cm root-mean-square error and -0.46cm average bias; however, it requires 666k parameters to implement a global grid.

There are several variants of IGGtrop [51, 54, 55]. The trade-offs between them related to the required number of parameters and the resulting accuracy. The experimental evaluation in this article employs the IGGtrop_SH variant [55]. This approach computes the coefficients a_0, a_1, a_2, a_3, a_4 for eqn. (3.10) using the empirical model:

$$a_0(h) = exp\left(\sum_{i=0}^{m} \alpha_i\, h^i\right), \tag{3.11}$$

$$a_j(h) = \sum_{i=0}^{5} \beta_{ji}\, h^i + c,\ \forall j \in \{1, 2, 3, 4\}, \tag{3.12}$$

where h is the altitude of the receiver. In eqn. (3.11), the parameter m is a function of the receiver latitude (see Section III in [55]). The coefficients α_j and β_{ji} are defined on a 2-D grid in latitude and longitude. These values were provided by the first author of [55]. The value of $T_z(t)$ is computed at the four nearest points on the 2-D grid and interpolate to compute its value at the receiver position.

3.2.4 Ionosphere Model

The ionosphere is the ionized zone of the atmosphere containing free electrons and positively charged ions. It ranges from about 50 km to 1000 km above the Earth surface. Electromagnetic signals are refracted in the ionosphere (Sec. 6.3 in [9]). It is a dispersive medium that impacts different frequencies, and the carrier and modulating signals, differently.

In GNSS OS processes, the dual-frequency user is able to form ionosphere-free combinations or estimate ionospheric delay using two measurements tracked for two frequencies from one satellite. The single-frequency users apply a prior model (i.e., Klobuchar for GPS and BeiDou [32, 34, 56], NeQuick for Galileo [33, 57]) using ionosphere parameters from the navigation message to reduce the ionosphere delay by about 50% Root Mean Square (RMS) [58, 59]. Real-time, single-frequency, PPP users compensate the ionosphere delay by processing ionosphere products. The correction of the ionosphere delay for the code measurement on frequency f by

$$\hat{I}^{s}_{f,r} = \frac{40.3}{f^2} STEC\ 10^{16}. \tag{3.13}$$

The Slant Total Electron Content (STEC) is calculated from a model of the Vertical Total Electron Content (VTEC). VTEC is computed at the Ionosphere Pierce Point (IPP), which is computed from the rover location $\mathbf{p}_r$ and the computed satellite location $\hat{\mathbf{p}}_s$.

SSR VTEC-SH: The agencies listed in Table 3.1 provide real-time VTEC SSR products that have global applicability. In the RTCM Version 3 standard [60], the real-time VTEC SSR message provides the parameters for a Spherical Harmonic (SH) expansion with degree of the expansion N, order of the expansion M, and coefficients $C_{n,m}$ and $S_{n,m}$ for $n = 0, \ldots, N$ and $m = 0, \ldots, M$. For

Table 3.1: Public real-time global ionosphere VTEC modeling services providing RTCM VTEC message. Each has NTRIP caster ID: ‘products.igs-ip.net:2101’.

Agency	SH degree	Mount point	References
CAS	15	SSRA00CAS0	[62]
CNES	12	SSRA00CNE0	[63]

a single-layer model, the VTEC model at the IPP is [10, 61]

$$VTEC(\phi_{PP},\lambda_{PP}) = \sum_{n=0}^{N} \sum_{m=0}^{min(n,M)} P_{n,m}(\sin(\phi_{PP})) \tag{3.14}$$

$$\cdot\,(C_{n,m}\cos(m\lambda_S) + S_{n,m}\sin(m\lambda_S)) \tag{3.15}$$

where $P_{n,m}()$ is the normalized associated Legendre function, (ϕ_{PP},λ_{PP}) are the geocentric latitude and longitude of the IPP, and λ_S is computed by

$$\lambda_S = (\lambda_{PP} + (t-50400)*\pi/43200)\,modulo\,(2\pi) \tag{3.16}$$

where t is the SSR epoch time of computation, modulo 86400 seconds.

The STEC is computed from VTEC using

$$STEC = \frac{VTEC}{sin(E+\phi_{PP})} \tag{3.17}$$

where E is the elevation angle of the satellite at the rover position.

US-TEC: For North America users, the National Oceanic and Atmospheric Administration (NOAA) provides the real-time US Total Electron Content (US-TEC) product for public usage [64]. US-TEC provides VTEC values in a uniform grid of point locations with 1 degree resolution in latitude and longitude. The official website (`https://services.swpc.noaa.gov/text/us-tec-total-electron-content.txt`) states that the normal update interval is 15 minutes, typically with 28 minutes latency. During the period from late 2020 through the middle of 2021, the latency was over 24 hours; therefore, although US-TEC is not used in the demonstration experiments which aim to real-time applications.

The VTEC at the IPP (within the geographical extent of the grid points) is computed as a linear function of the values at grid points. The VN-DGNSS server uses distance weighted spatial interpolation [65,66]:

$$VTEC(IPP) = \mathbf{w}(IPP)\, \mathbf{I}^G, \tag{3.18}$$

where $\mathbf{w}(IPP)$ is a vector of weights. Both $\mathbf{w}(IPP)$ and $\mathbf{I}^G$ are vectors with K components. The k-th element w_k of the weighting vector determines the amount that a VTEC value $[\mathbf{I}^G]_k$ at the k-th grid point IPP_k contributes to the value of Total Electron Content (TEC) at the desired IPP.

The vector $\mathbf{w}(IPP) = [w_1, ..., w_K]$ satisfies the following constraints:

1. $\sum_{i=1}^{K} w_k = 1$, so that Eqn. (3.18) interpolates the value for VTEC from the grid points.
2. the k-th element w_k should decrease smoothly as $d_k = \|IPP - IPP_k\|$ increases. This results in a smooth interpolation between the grid point values.

The approach herein uses at most four nonzero weights. If $IPP = IPP_k$ for some k, then $w_k = 1$ and all remaining values of $\mathbf{w}(IPP)$ are zero. Otherwise, the IPP is between four grid points. In this case, we define $a \in \Re^K$ such that $a_k = 1/d_k$ for those four corner grid points, noting that a_k is finite because $d_k \neq 0$. All the remaining elements of $\mathbf{a}$ are zero. Then, the components of $\mathbf{w}(IPP)$ are defined as $w_k = \frac{a_k}{\sum_{i=1}^{K} a_i}$.

Spatial interpolation provides the VTEC at the IPP. The STEC is computed as [66]:

$$STEC = F(E)VTEC(IPP). \tag{3.19}$$

where $F(E)$ is the ionospheric obliquity factor defined as

$$F(E) = \frac{1}{\sqrt{1 - \left[\frac{r_e \cos(E)}{r_e + h_m}\right]^2}}, \tag{3.20}$$

where r_e is the average radius of the earth, and h_m is the height of the maximum electron density (assumed herein to be 350 km).

3.2.5 RT-PPP Corrections and the Corrected Code Model

This section discusses the choice of RT-PPP corrections used herein to mitigate the CME effects. The PPP SSR format corrections are communicated via parameters for models of each component of the CME. They demonstrate efficacy on a global scale. Various sources are available. These sources have been comprehensively defined and examined in [10, 12, 48, 51]. The real-time orbit and clock products are corrections to the satellite position and clock error from broadcast ephemeris. In this study, we choose to use those from WHU. Satellite hardware bias could be corrected using either DCB or OSB format corrections. The multi-GNSS OSB products are more convenient. In this study, the OSB products are provided by CAS. Tropospheric delay is corrected by the global *IGGtrop* empirical model. Ionospheric delay is compensated using the real-time global VTEC product provided by CNES. The model and the reasons for choosing it are discussed in Section IV.D of [12].

The RT-PPP corrections related to satellite orbit and clock, satellite hardware bias, and tropospheric delay can achieve centimeter-level accuracy. The assessment of the CNES VTEC product indicates that the RMS ranges from 2.07 to 6.15 TEC Units (TECU), which, when scaled using the GPS L1 frequency, corresponds to 0.34 to 1.00 meters [67].

By mitigating the CME, the corrected code model can be represented as:

$$\begin{aligned}\delta\rho^s_{SSR} &= \rho^s_{f,r}(t_r) + c\,\hat{dt}^s - \hat{\delta}^s - \hat{B}^s_f - \hat{T}^s_r - \hat{I}^s_{f,r} \\ &= R(\mathbf{p}_r, \tilde{\mathbf{p}}_s) + \Delta^\gamma_{r,SSR} + M^s_{r,SSR} + \varepsilon^s_{r,SSR} \qquad (3.21)\end{aligned}$$

where $\Delta^\gamma_{r,SSR} = \Delta^\gamma_r$, M^s_r, and

$$\begin{aligned}\varepsilon^s_{r,SSR} &= R(\mathbf{p}_r, \mathbf{p}_s) - R(\mathbf{p}_r, \tilde{\mathbf{p}}_s) + \delta^s - \hat{\delta}^s + B^s_f - \hat{B}^s_f \\ &\quad + T^s_r - \hat{T}^s_r + I^s_{f,r} - \hat{I}^s_{f,r} + \eta^s_{r,\rho} \qquad (3.22)\end{aligned}$$

represents the residual of CME and measurement noise.

3.3 VN-DGNSS

This section present the VN-DGNSS approach that provides a Multi-GNSS correction service to users [12]. The RTCM OSR messages that are transmitted are accepted by most receivers. In this approach, there is no need for additional *physical* reference stations. The RTCM OSR format communicates corrections in the form of an observation, which must be computationally constructed in any VN-DGNSS approach using PPP information. The computationally constructed observation requires the satellite position and time-of-transmissions for each satellite to be consistent for measurements at a specified time at the user-specified location.

At present, few receivers are available that accept SSR correction information. Even as more receivers become available that accept SSR correction information, legacy receivers will require correction information in OSR format. The RTCM format for communicating OSR correction information is as a measurement.

Considering eqn. (3.1) from the perspective of constructing an RTCM OSR message using SSR data for a known virtual base antenna position $\mathbf{p}_b$. First, the base station receiver clock bias Δ_b^γ is not important for positioning applications. This error will only affect the estimated rover clock bias, since it is identical for all code measurements of constellation γ. Therefore, for the virtual base station, Δ_b^γ is set to zero. Second, the multipath and receiver terms $(M_b^s + \eta_{b,\rho}^s)$ are non-CME and should not be included. Therefore, the desired code measurement to send as an RTCM OSR message is modeled as

$$\rho_{f,b}^s(t_b) = R(\mathbf{p}_b, \hat{\mathbf{p}}_s) + E_b^s - \Delta^s + B_f^s + T_b^s + I_{b,f}^s. \tag{3.23}$$

The server (i.e., Virtual Reference Station (VRS)) transmits RTCM 3.X messages to the receiver which include the virtual base station position $\mathbf{p}_b$ and time t_b, and the computed code measurements $\rho_{f,b}^s(t_b)$. The code measurement construction can be decomposed into two parts: range component $R(\mathbf{p}_b, \hat{\mathbf{p}}_s)$ and CME terms. The CME corrections are computed by the models discussed in Sec. 3.2.

To compute the term $R\Big(\mathbf{p}_b, \hat{\mathbf{p}}_s\Big)$ in eqn. (3.23) when the base location $\mathbf{p}_b$ and measurement time t_b are given. This computation must determine the location $\hat{\mathbf{p}}_s(t_s)$ for which the signal received from satellite s transmitted at time t_s would be received at time t_b by a virtual receiver at location

$\mathbf{p}_b$. These computations will neglect the common-mode errors, whose effect is analyzed in Section 3.3.2.

For a signal pseudo-transmit-time $\hat{t}_s$, the ICD provides equations and the broadcast navigation message provides data to compute the satellite clock offset $\hat{dt}^s(\hat{t}_s)$, satellite position $\hat{\mathbf{p}}_s(\bar{t}_s)$ and satellite velocity $\hat{\mathbf{v}}_s(\bar{t}_s)$, where $\bar{t}_s = (t_b - t_p^s - \hat{dt}^s)$ is the time-of-signal-transmission corrected by the navigation satellite clock error model from the ICD where t_p^s is the pseudo propagation time.

3.3.1 Algorithm Definition

The range between the satellite and virtual base antennae can be computed in two ways:

$$R\Big(\mathbf{p}_b, \hat{\mathbf{p}}_s(t_b - t_p^s - \hat{dt}^s)\Big) \text{ and } c\ (t_p^s + \hat{dt}^s) \tag{3.24}$$

Algorithm 1 adjusts the (uncorrected) propagation time t_p^s to compute the satellite position $\hat{\mathbf{p}}_s(\bar{t}_s)$ at the corrected time of transmission $\bar{t}^s$ by minimizing the error between the two range equations:

$$F(t_p^s : \mathbf{p}_b, t_b) = R\Big(\mathbf{p}_b, \hat{\mathbf{p}}_s(t_b - t_p^s - \hat{dt}^s)\Big) - c\ (t_p^s + \hat{dt}^s). \tag{3.25}$$

The quantity $t_g^s = t_p^s + \hat{dt}^s$ is the geometric travel time. The notation $F(t_p^s : \mathbf{p}_b, t_b)$ means that t_p^s is the argument and $\mathbf{p}_b$ and t_b are known parameters.

The optimization is implemented using numeric search. Step 1 initializes the propagation time to $t_p^s = 0.067$ seconds because GNSS satellites are approximately 20,000 km from the Earth surface. Step 2 declares a parameter to store the last value of t_p^s. Step 3 starts the while loop which terminates when $|t_p^- - t_p^s|$ is small. Step 4 computes the pseudo-transmit time $\hat{t}^s$, which is used in

Step 5 to compute the satellite clock correction $\hat{dt}^s(\hat{t}_s)$, and the position $\hat{\mathbf{p}}_s(\bar{t}_s)$ and velocity $\hat{\mathbf{p}}_s(\bar{t}_s)$. The ICD models are represented by the function $f(\hat{t}_s, \boldsymbol{\theta}_e^s)$ where $\boldsymbol{\theta}_e^s$ are the broadcast ephemeris and clock correction parameters. Steps 6 - 9 compute the two ranges and the range error for the current value of t_p^s. Step 10 computes the partial derivative of the cost with respect to the t_p^s

$$\frac{\partial F}{\partial t_p^s} = -\left(\mathbf{1}_b^s \cdot \hat{\mathbf{v}}_s(\bar{t}_s) + c\right)\left(1 - a_1 - 2a_2\left(\hat{t}_s - t_{oc}\right)\right), \tag{3.26}$$

where a_1, a_2, and t_{oc} are the clock model parameters from the navigation message. Step 11 stores the t_p^s to t_p^- before updating t_p^s Step 12 implements Newton's Zero Finding Algorithm to optimize t_p^s to minimize the square of the error defined in Eqn. (3.25). Step 14 computes satellite transmission time $\bar{t}_s$ which will be used as t_s in the SSR clock product of Sec. 3.2.1.

For the input receiver time t_b and base station location $\mathbf{p}_b$, this optimization process provides the broadcast clock correction $\hat{dt}^s(\hat{t}^s)$ and the satellite location $\hat{\mathbf{p}}_s(\bar{t}_s)$ at the corrected time of transmission. These enable computation of $R\Big(\mathbf{p}_b, \hat{\mathbf{p}}_s(\bar{t}_s)\Big)$ as required for the RTCM OSR measurement defined in eqn. (3.23).

3.3.2 Effect of Common Mode Errors

At the user receiver, residual measurements are formed for both the base and user receiver measurements. For the base measurements, the available information is t_b and $\rho_{f,b}^s(t_b)$. The user receiver computes the time of satellite transmission as

$$\tilde{t}_s = t_b - \frac{1}{c}\rho_{f,b}^s(t_b),$$

Algorithm 1 Satellite Position Estimation

```
Input: $\mathbf{p}_b$, $t_b$.
Output: $\hat{\mathbf{p}}_s(t_s)$, $\hat{v}_s(t_s)$, $\hat{dt}^s$ and $t_s$.
$t_p^s = 0.067$;                                         // Initialize the propagation time
$t_p^- = 0$;                                             // Initialize previous value to 0
while $|t_p^- - t_p^s| > 10^{-11}$ do
    $\hat{t}_s = t_b - t_p^s$;                           // Pseudo-transmit-time
    $[\hat{\mathbf{p}}_s(\bar{t}_s), \hat{\mathbf{v}}_s(\bar{t}_s), \hat{dt}^s(\hat{t}_s)] = f(\hat{t}_s, \boldsymbol{\theta}_e^s)$;    // ICD models
    $R_1 = R(\mathbf{p}_b, \hat{\mathbf{p}}_s(\bar{t}_s))$     // Range based on position
    $t_g^s = t_p^s + \hat{dt}^s(\hat{t}_s)$              // See definition in Eqn. (3.25)
    $R_2 = c \cdot t_g^s$                                // Range based on geometric travel time
    $F = R_1 - R_2$;                                     // Eqn. (3.25)
    $dF = -\left(\frac{\hat{\mathbf{v}}_s(\bar{t}_s)\cdot(\hat{\mathbf{p}}_s - \mathbf{p}_b)}{R_1} + c\right)\left(1 - \frac{\partial}{\partial t_p^s}\hat{dt}^s(\hat{t}_s)\right)$;    // Eqn. (3.26)
    $t_p^- = t_p^s$;                                     // save the previous value
    $t_p^s = t_p^s - \frac{F}{dF}$;                      // Newton's Zero Finding Algorithm
end while
$\bar{t}_s = t_b - t_p^s - \hat{dt}^s(\hat{t}_s)$.      // Transmit time by the satellite clock
```

where $\tilde{t}_p^s = \frac{1}{c}\rho_{f,b}^s(t_b)$ is the measured propagation time. Because the measurement of $\rho_{f,b}^s(t_b)$ includes errors, as modeled in Eqn. (2.1), the measured and actual values of the transmit time are related according to

$$\tilde{t}_s = \bar{t}_s - e_b^s,$$

where e_b^s denotes both CME and non-CME scaled to units of time (i.e., $|e_b^s| \leq 200$ ns). The error e_b^s is neglected in the algorithm of the previous section. This section analyzes the effect of this decision on the satellite position and its range from the base.

The algorithm computes $\mathbf{p}_s(\bar{t}_s)$ when it should have computed $\mathbf{p}_s(\bar{t}_s - e_b^s)$. Consider the Taylor series expansion:

$$\mathbf{p}_s(\bar{t}_s - e_b^s) = \mathbf{p}_s(\bar{t}_s) - \left.\frac{\partial}{\partial t}\mathbf{p}_s(t)\right|_{t=\bar{t}_s} e_b^s \tag{3.27}$$

$$= \mathbf{p}_s(\bar{t}_s) - \mathbf{v}_s(\bar{t}_s)\, e_b^s \tag{3.28}$$

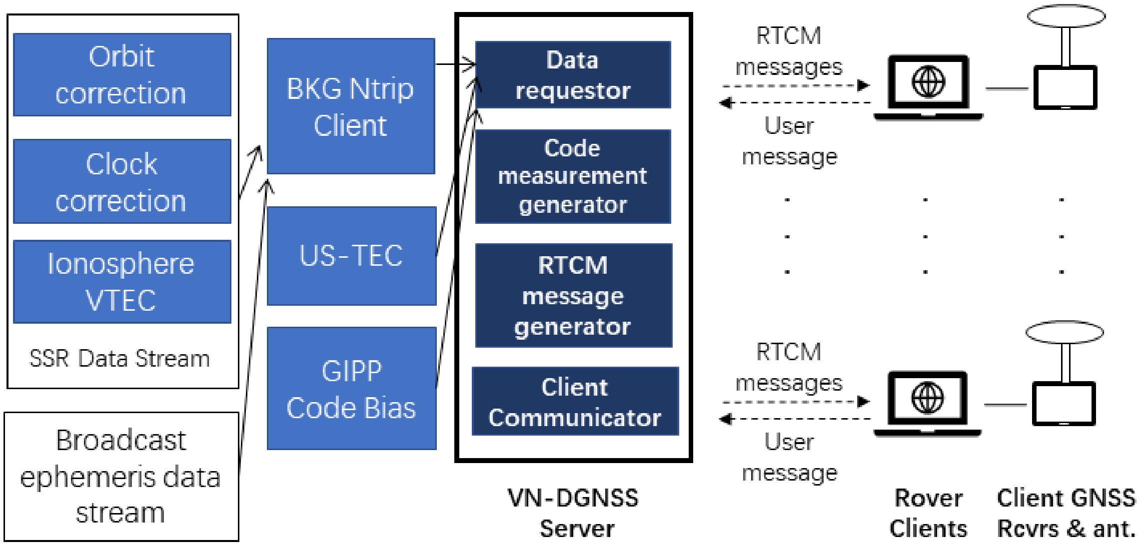

Figure 3.1: VN-DGNSS server-client architecture

Therefore, because the satellite speed is about 4,000 m/s and $|e_b^s| \leq 2 \times 10^{-7}$, the effect of neglecting e_b^s on the satellite position calculation is less than one millimeter.

3.3.3 VN-DGNSS Server-Client System Design

This section describes the software implementation for a publicly available, open-source, client/server VN-DGNSS implementation with global coverage. The VN-DGNSS repository is public on GitHub: `https://github.com/Azurehappen/Virtual-Network-DGNSS-Project`. The server receives real-time information in SSR format and provides each client with virtual base station RTCM OSR formatted messages applicable to their local vicinity for BeiDou B1, GALILEO E1, and GPS L1. This approach eliminates the need for the client to have physical access to a local reference station.

3.3.3.1 System Architecture

Fig. 3.1 displays the VN-DGNSS client/server framework. The VN-DGNSS server includes four fundamental components.

- The *data requestor* establishes communications with online sources to maintain real-time SSR data. The BKG NTRIP Client (BNC) [68] provides broadcast ephemeris for each satellite system, Multi-GNSS SSR orbit and clock corrections, and SSR VTEC information (see Table 3.1). US-TEC products are included as an option for US clients. CAS GIPP provides code bias products [49]. Because the IGGtrop_SH parameters are static, they are loaded at run-time and do not require real-time communications.

- The *code measurement generator* constructs the code measurements, for the virtual base position $\mathbf{p}_b$ requested by the client, using eqn. (3.23) for GPS L1, Galileo E1 and Beidou B1. The range is computed as described in Sec. 3.3.1. The correction terms in the second line of eqn. (3.23) are computed using the models discussed in Sec. 3.2.

- The *RTCM message generator* creates RTCM message type 1004 and MSM4 message types: 1074 for GPS, 1094 for Galileo, 1124 for BeiDou. The RTCM 1004 message communicates the virtual reference station position $\mathbf{p}_b$. The RTCM MSM4 message includes the code measurements constructed by the code measurement generator at integer epoch times t_b (i.e., 1.0 Hertz), along with the observation type and Signal-to-Noise Ratio (SNR)[1].

- The *client communicator* receives requests from, then establishes and maintains TCP connections with clients. In addition to its internet address, the client sends its (desired) virtual

---

[1] In the current implementation, the server computes the SNR as $floor(\frac{A\,E}{\pi}) + \underline{S}$, where E is the satellite elevation in radians, $\underline{S}$ is the minimum SNR, and A is a coefficient that determines the maximum SNR.

reference station position $\mathbf{p}_b$, and the GNSS constellations and the observation types for which the client desires RTCM messages. Clients that are moving can update their desired virtual reference station position as necessary to keep it within a reasonable distance (e.g., 20 km) of their location.

Some portions of the VN-DGNSS (e.g., code measurement generator, RTCM message generator) are modifications of open-source functions in RTKLIB [69] and BNC [68].

3.3.3.2 Implementation Strategies

Details and choices required for the VN-DGNSS server implementation are described below.

1. Table 3.1 list the two agencies that currently stream SSR Multi-GNSS corrections and global VTEC SH parameters using RTCM messages through NTRIP. Both are available through the server.

2. The real-time orbit and clock corrections are applicable to a specific Issue Of Data (IOD) ephemeris. GPS and Galileo ephemeris provides the IOD number for each satellite. The Beidou IOD depends on the agency providing the data. The two agencies in Table 3.1 both share the same methodology (see `http://www.ppp-wizard.net/news.html`):

$$BeiDou\ IOD = ((int)toe/720)\ modulo\ 240,$$

   where *toe* is the time-of-ephemeris in the BeiDou navigation message.

3. The multi-GNSS OSB product provided by CAS [49] is referred to as GIPP. The GIPP code bias data can be downloaded from `ftp://ftp.gipp.org.cn/product/dcb/daybias/`. They are updated with a period of one day update and latency of 1-5 days. The two agencies listed in Table 3.1 also provide code biases through NTRIP; however, they do not provide bias estimates for all observation types required for the experiments.

4. The SSR data has two types: Antenna Phase Centre (APC) and Center of Mass (COM). The broadcast ephemeris is referred to the satellite's APC; therefore, the selected SSR data stream for orbit corrections must also reference to the APC, not COM.

Chapter 4

Linear State Estimation

This article focuses on outlier recommendation for GNSS applications in linear systems. State estimation will be performed using multi-GNSS SF code and Doppler measurements. This section outlines the position, velocity, acceleration (PVA) state propagation model and the measurement update using the linearized code measurement model and the Doppler measurement model.

4.1 Time Propagation

The state vector is defined as

$$\mathbf{x} = [\mathbf{p}_r, \mathbf{v}_r, \mathbf{a}_r, \boldsymbol{\Delta}^{\gamma}, r_c]^{\top} \in \Re^n \tag{4.1}$$

where $\mathbf{a}_r \in \Re^3$ denotes the receiver acceleration, $\boldsymbol{\Delta}^{\gamma} \in \Re^{n_s}$ represents the vector of receiver clock biases for the n_s different GNSS constellations. The state at time $t_k = kT$ will be denoted as $\mathbf{x}_k$ where T is the sampling interval.

The time update portion of the discrete-time model is

$$\mathbf{x}_{k+1} = \mathbf{F}\mathbf{x}_k + \mathbf{w}_k \tag{4.2}$$

is a standard PVA approach where the state transition matrix is

$$\mathbf{F} = \begin{bmatrix} \mathbf{I}_3 & T\mathbf{I}_3 & \frac{1}{2}T^2\mathbf{I}_3 & \mathbf{0} & \mathbf{0} \\ \mathbf{0} & \mathbf{I}_3 & T\mathbf{I}_3 & \mathbf{0} & \mathbf{0} \\ \mathbf{0} & \mathbf{0} & \mathbf{I}_3 & \mathbf{0} & \mathbf{0} \\ \mathbf{0} & \mathbf{0} & \mathbf{0} & \mathbf{I}_{n_s} & \mathbf{T}_{n_s} \\ \mathbf{0} & \mathbf{0} & \mathbf{0} & \mathbf{0} & 1 \end{bmatrix} \tag{4.3}$$

and $\mathbf{w}_k \sim \mathcal{N}(\mathbf{0}, \mathbf{Q}_d)$ is the white Gaussian process noise (see eqn. (B.5) in Appendix B for the derivation of $\mathbf{Q}_d$), $\mathbf{I}_q$ represents the identity matrix with q rows and columns, and $\mathbf{T}_{n_s}$ is a column vector with n_s elements all having value of T. The symbol $\mathbf{0}$ is a conformal matrix containing all zeros.

The time propagation model for the state estimate is:

$$\hat{\mathbf{x}}_{k+1}^{-} = \mathbf{F}\hat{\mathbf{x}}_k^{+}, \tag{4.4}$$

$$\mathbf{P}_{k+1}^{-} = \mathbf{F}\mathbf{P}_k^{+}\mathbf{F}^{\top} + \mathbf{Q}_d \tag{4.5}$$

where $\hat{\mathbf{x}}_k^{-}$ and $\hat{\mathbf{x}}_k^{+}$ denote the prior and posterior state estimate, and $\mathbf{P}_k^{-}$ and $\mathbf{P}_k^{+}$ denote the prior and posterior state estimate error covariance matrix. The Probability Density Function (PDF) of prior state $\mathbf{x}_k$ is assumed to be Gaussian $\mathbf{x}_k \sim \mathcal{N}(\hat{\mathbf{x}}_k^{-}, \mathbf{P}_k^{-})$. Outliers are not directly involved in the time propagation process since they only affect the measurements, the outlier accommodation is considered in the measurement update process.

4.2 Measurement Models

The measurement vector $\mathbf{y}$ at time k is modeled as:

$$\mathbf{y}_k = \mathbf{H}\mathbf{x}_k + \boldsymbol{\eta}_k \tag{4.6}$$

where $\mathbf{y}_k \in \Re^m$, $\mathbf{H} \in \Re^{m\times n}$ is the known measurement matrix, and $\boldsymbol{\eta}_k \sim \mathcal{N}(\mathbf{0}, \mathbf{R})$ is white Gaussian measurement noise. The covariance matrix $\mathbf{R} \in \Re^{m\times m}$ is assumed to be invertible and diagonal; therefore, it can be written as $\mathbf{R} = \sum_{i=1}^{m} \sigma_i^2 \mathbf{e}_i \mathbf{e}_i{}^{\top}$, where $\mathbf{e}_i$ is i-th standard basis vector. The prior, process noise, and measurement noise are independent.

Some of the measurements will be affected by outliers. Outlier measurements are those that are very unlikely given the model stated in eqn. (4.6). When the i-th measurement at time k is affected by an outlier, that measurement is modeled as

$$y_i(k) = \mathbf{h}_i \mathbf{x}_k(k) + \eta_i + s_i(k), \tag{4.7}$$

where $s_i(k)$ represents the outlier and $\mathbf{h}_i$ is the i-th row of $\mathbf{H}$. There is usually no known model for the outlier $s_i(k)$. The objective is to use the measurements $\mathbf{y}_k$ to estimate the state vector while attenuating the effects of the outlier vector $\mathbf{s}_k$. The GNSS code measurement outlier will be defined in Sec. 4.3.

Using eqn. (2.5), the linearized code measurement model can be computed as

$$\begin{aligned} z_s &= \delta\rho^s - R(\mathbf{p}^-, \hat{\mathbf{p}}_s) + (\mathbf{1}_r^s)^\top \mathbf{p}^- \\ &= (\mathbf{1}_r^s)^\top \mathbf{p}_r + \Delta_{r,tech}^{\gamma} + M_{r,tech}^s + \varepsilon_{r,tech}^s \\ &= \mathbf{h}_s^{\rho} \mathbf{x} + M_{r,tech}^s + \varepsilon_{r,tech}^s \end{aligned} \tag{4.8}$$

where $\Delta_{r,tech}^{\gamma}$, $M_{r,tech}^s$, and $\varepsilon_{r,tech}^s$ denote $\Delta_{r,OSR}^{\gamma}$, $M_{r,OSR}^s$, and $\varepsilon_{r,OSR}^s$ in DGNSS applications or $\Delta_{r,SSR}^{\gamma}$, $M_{r,SSR}^s$, and $\varepsilon_{r,SSR}^s$ in PPP applications, and

$$\mathbf{h}_s^{\rho} = [(\mathbf{1}_r^s)^\top, \mathbf{0}_{1\times 3}, \mathbf{0}_{1\times 3},\ \mathbf{e}_{\gamma}^\top,\ 0] \tag{4.9}$$

After compensating for the satellite velocity and clock drift to eqn. (2.7), the linear Doppler measurement for satellite s is modeled as

$$\begin{aligned} \delta D_s &= (\mathbf{1}_s^r)^\top \mathbf{v}_r + r_c + \eta_D^s \\ &= \mathbf{h}_s^D \mathbf{x} + \eta_D^s \end{aligned} \tag{4.10}$$

where

$$\mathbf{h}_s^D = [\mathbf{0}_{1\times 3}, (\mathbf{1}_r^s)^\top, \mathbf{0}_{1\times 3}, \mathbf{0}_{1\times n_s}, 1]. \tag{4.11}$$

In the case of DGNSS, $\dot{\Delta}$ and η_D^s denote the single-differenced receiver clock drift and Doppler measurement noise. Therefore, the measurement vector $\mathbf{y}$ is defined as

$$\mathbf{y} = [\mathbf{z}^\top, \mathbf{D}^\top]^\top \in \Re^m \tag{4.12}$$

where $\mathbf{z} = [z_1, ..., z_{m_s}]^\top$ and $\mathbf{D} = [\delta D_1, ..., \delta D_{m_s}]^\top$ for m_s satellites and $m = 2m_s$. The measurement matrix is defined as

$$\mathbf{H} = [\mathbf{H}^\rho; \mathbf{H}^D] \tag{4.13}$$

where $\mathbf{H}^\rho = [\mathbf{h}_1^\rho; ...; \mathbf{h}_{m_s}^\rho]$ and $\mathbf{H}^D = [\mathbf{h}_1^D; ...; \mathbf{h}_{m_s}^D]$.

The measurement noise matrix is defined as

$$\mathbf{R} = \mathrm{diag}[\sigma_{1,\rho}^2, ..., \sigma_{m_s,\rho}^2, \sigma_{1,D}^2, ..., \sigma_{m_s,D}^2]. \tag{4.14}$$

4.3 Measurement Noise Model and Outliers

In GNSS applications, the multipath or non-LOS errors cause principally due to signal travel through reflecting structures and ground. In the case of code measurement, it is capable to reach a theoretical value of 1.5 times the wavelength, which means the worst case for GPS C/A code (its wavelength $\approx$ 293.1m) can reach 450 meters [70]. In most open-sky cases, they are less than 3 meters.

The state estimation process assumes that the combined effect of measurement noise plus multipath and nonline-of-sight errors follows a white Gaussian distribution with $(M^s_{r,tech} + \varepsilon^s_{r,tech}) \sim \mathcal{N}(0, \sigma^2_{s,\rho})$ where $\sigma_{s,\rho}$ signifies the measurement noise in this section.

This assumption is reasonable under open-sky conditions where multipath effects are generally minor [71, 72]. However, in challenging urban scenarios, such as areas with narrow lanes flanked by densely tall buildings and trees, numerous GNSS signals are obstructed or suffer from anomalies like multipath and non-line-of-sight effects, resulting from reflections. In this situation, multipath and non-LOS effects may increase to tens of meters [73]. Given the absence of a definitive model for these errors, they are treated as outliers when they are significant.

4.4 Measurement Update by MAP Estimation

This section first reviews MAP estimation using all measurements. Then it introduces a convenient approach for selecting or weighting measurements so that various robust estimation approaches can be compared using a unified notation.

4.4.1 Estimation using All Measurements

Under the assumption that all measurements are devoid of outliers, the MAP approach chooses the state estimate $\hat{\mathbf{x}}$ to maximize the conditional probability density (see [74]):

$$\hat{\mathbf{x}}_k = \underset{\mathbf{x}_k}{\operatorname{argmax}}\ p(\mathbf{x}_k|\mathbf{y}_k) = \underset{\mathbf{x}_k}{\operatorname{argmax}}\ p(\mathbf{y}_k|\mathbf{x}_k)p(\mathbf{x}_k). \tag{4.15}$$

Minimizing the negative log-likelihood, using the assumption that the prior and noise are Gaussian, yields the cost function:

$$\begin{aligned}\hat{\mathbf{x}}_k &= \underset{\mathbf{x}_k}{\operatorname{argmin}} \left[(\mathbf{y}_k - \mathbf{H}\mathbf{x}_k)^\top \mathbf{R}^{-1}(\mathbf{y}_k - \mathbf{H}\mathbf{x}_k) + (\mathbf{x}_k - \hat{\mathbf{x}}_k^-)^\top (\mathbf{P}_k^-)^{-1}(\mathbf{x}_k - \hat{\mathbf{x}}_k^-)\right] \\ &= \underset{\mathbf{x}_k}{\operatorname{argmin}} \|\boldsymbol{\Sigma}_{\mathbf{R}}(\mathbf{y}_k - \mathbf{H}\mathbf{x}_k)\|_2^2 + \|\boldsymbol{\Sigma}_{\mathbf{P}}(\mathbf{x}_k - \hat{\mathbf{x}}_k^-)\|_2^2 \end{aligned} \tag{4.16}$$

where $\mathbf{R}^{-1} = \boldsymbol{\Sigma}_{\mathbf{R}}{}^\top \boldsymbol{\Sigma}_{\mathbf{R}}$ and $(\mathbf{P}_k^-)^{-1} = \boldsymbol{\Sigma}_{\mathbf{P}}{}^\top \boldsymbol{\Sigma}_{\mathbf{P}}$. [1] Solving eqn. (4.16) for $\mathbf{x}_k$ and dropping the k subscripts, yields the estimate

$$\hat{\mathbf{x}} \doteq \left(\mathbf{H}^\top \mathbf{R}^{-1}\mathbf{H} + \mathbf{J}^-\right)^{-1} \left(\mathbf{H}^\top \mathbf{R}^{-1}\mathbf{y} + \mathbf{J}^- \hat{\mathbf{x}}^-\right) \tag{4.17}$$

where $\mathbf{J}^- = (\mathbf{P}^-)^{-1}$ is the *prior information matrix*. Eqn. (4.17) is the Kalman filter measurement update in Information Form. In this expression, $\mathbf{J}^+ = \mathbf{H}^\top \mathbf{R}^{-1}\mathbf{H} + \mathbf{J}^-$ is the *posterior information matrix* and $\mathbf{P}^+ = (\mathbf{J}^+)^{-1}$ is the *posterior error covariance matrix*.

4.4.2 Estimation using Selected Measurements

For the purpose of comparing approaches for excluding or de-weight the measurements, it is convenient to introduce the vector of measurement selection variables $\mathbf{b} = [b_1, b_2, ..., b_m]^\top$. When the vector $\mathbf{b}$ is defined to be a binary vector where $b_i \in \{0, 1\}$, it is used to select certain measurements to be used ($b_i = 1$) and others to be ignored ($b_i = 0$) (see [75, 76]). Alternatively, when the vector $\mathbf{b}$ is a non-binary vector where $b_i \in [0, 1]$, b_i can be looked upon as a means to de-weight the i-th measurement. Corresponding to $\mathbf{b}$, define the diagonal matrix $\boldsymbol{\Phi}(\mathbf{b}) = diag(\mathbf{b})$.

---

[1] The notation $\|\mathbf{v}\|_{\mathbf{P}}^2 = \mathbf{v}^\top \mathbf{P}^{-1}\mathbf{v} = \|\boldsymbol{\Sigma}_{\mathbf{P}}\mathbf{v}\|_2^2$, where $\mathbf{P}^{-1} = \boldsymbol{\Sigma}_{\mathbf{P}}^\top \boldsymbol{\Sigma}_{\mathbf{P}}$ for $\boldsymbol{\Sigma}_{\mathbf{P}} > \mathbf{0}$. This Mahalanobis norm naturally arises with Gaussian distributions.

When $\mathbf{b} = \mathbf{1}$ (i.e., each $b_i = 1$), then $\boldsymbol{\Phi}(\mathbf{1}) = \mathbf{I}$ and eqn. (4.16) yields the same estimate as the solution of

$$\hat{\mathbf{x}}_{\mathbf{b}} = \underset{\mathbf{x}}{\operatorname{argmin}} \Big(\|\boldsymbol{\Sigma}_{\mathbf{R}}\, \boldsymbol{\Phi}(\mathbf{b})\, (\mathbf{y} - \mathbf{H}\mathbf{x})\|_2^2 + \|\boldsymbol{\Sigma}_{\mathbf{P}^-}\, (\mathbf{x} - \hat{\mathbf{x}}^-)\|_2^2 \Big). \tag{4.18}$$

In the case, where some elements of $\mathbf{b}$ are set to zero, the matrix $\boldsymbol{\Phi}(\mathbf{b})$ has the effect of removing those rows of both $\mathbf{y}$ and $\mathbf{H}$ from the optimization. Alternatively, in the case where the elements of $\mathbf{b}$ are values in [0, 1], the matrix $\boldsymbol{\Phi}(\mathbf{b})$ has the effect of de-weight the rows of both $\mathbf{y}$ and $\mathbf{H}$ during the optimization. Each choice of $\mathbf{b}$ results in a different estimate $\hat{\mathbf{x}}_{\mathbf{b}}$.

By defining:

$$\mathbf{A}_{\mathbf{b}} = \begin{bmatrix} \boldsymbol{\Sigma}_{\mathbf{R}}\, \boldsymbol{\Phi}(\mathbf{b})\, \mathbf{H} \\ \\ \boldsymbol{\Sigma}_{\mathbf{P}^-} \end{bmatrix}, \quad \mathbf{c}_{\mathbf{b}} = \begin{bmatrix} \boldsymbol{\Sigma}_{\mathbf{R}}\, \boldsymbol{\Phi}(\mathbf{b})\, \mathbf{y} \\ \\ \boldsymbol{\Sigma}_{\mathbf{P}^-}\, \hat{\mathbf{x}}^- \end{bmatrix} \tag{4.19}$$

the cost function in eqn. (4.18) can be written as:

$$C(\mathbf{x}, \mathbf{b}) = \|\mathbf{A}_{\mathbf{b}}\, \mathbf{x} - \mathbf{c}_{\mathbf{b}}\|^2, \tag{4.20}$$

which, for any given $\mathbf{b}$, is a Least Squares problem that can be solved for $\mathbf{x}$. Minimizing the cost function in eqn. (4.20) with respect to $\mathbf{x}$ for a fixed $\mathbf{b}$ yields:

$$\begin{aligned} \hat{\mathbf{x}}_{\mathbf{b}} &= (\mathbf{A}_{\mathbf{b}}^\top \mathbf{A}_{\mathbf{b}})^{-1} \mathbf{A}_{\mathbf{b}}^\top \mathbf{c}_{\mathbf{b}} \\ &= \Big[\mathbf{H}^\top \boldsymbol{\Phi}(\mathbf{b})^\top \mathbf{R}^{-1} \boldsymbol{\Phi}(\mathbf{b}) \mathbf{H} + (\mathbf{P}^-)^{-1}\Big]^{-1} \Big[\mathbf{H}^\top \boldsymbol{\Phi}(\mathbf{b})^\top \mathbf{R}^{-1} \boldsymbol{\Phi}(\mathbf{b}) \mathbf{y} + (\mathbf{P}^-)^{-1} \hat{\mathbf{x}}^-\Big]. \end{aligned} \tag{4.21}$$

The posterior information matrix corresponding to the measurement selection vector $\mathbf{b}$ is

$$\mathbf{J}_{\mathbf{b}}^{+} \doteq \mathbf{H}^{\top}\mathbf{\Phi}(\mathbf{b})^{\top}\mathbf{R}^{-1}\mathbf{\Phi}(\mathbf{b})\mathbf{H} + (\mathbf{P}^{-})^{-1}. \tag{4.22}$$

Using the decomposition of $\mathbf{R}$ discussed after eqn. (4.6), the cost function and posterior information can be expressed as:

$$C(\mathbf{x},\mathbf{b}) = \|\mathbf{x} - \hat{\mathbf{x}}^{-}\|^{2}_{\mathbf{P}^{-}} + \sum_{i=1}^{m} \frac{b_i^2}{\sigma_i^2}(y_i - \mathbf{h}_i\mathbf{x})^2, \text{ and} \tag{4.23}$$

$$\mathbf{J}_{\mathbf{b}}^{+} = \sum_{i=1}^{m} \frac{b_i^2}{\sigma_i^2}\mathbf{h}_i^{\top}\mathbf{h}_i + \mathbf{J}^{-}. \tag{4.24}$$

This form is convenient for highlighting some inherent trade-offs. If $\mathbf{b} = \mathbf{0}$, the solution is the prior and the cost function has value zero; however, no information is extracted from the measurements so $\mathbf{J}_{\mathbf{b}}^{+} = \mathbf{J}^{-}$. For each b_i that is switched from 0 to 1, both the cost and information matrix increase due to the new term in each summation. The added cost of measurement i is computed as a function of its residual $r_i = y_i - \mathbf{h}_i\mathbf{x}$. If $\mathbf{b} = \mathbf{1}$, the solution using all measurements is the same as that in eqn. (4.17). For all other cases (i.e., $\mathbf{b}$ not equal to $\mathbf{0}$ of $\mathbf{1}$), the goal in deciding which measurements to use is to achieve a good trade-off between increased information (quantified by the first term of $\mathbf{J}_{\mathbf{b}}^{+}$) and increased cost $C(\mathbf{x},\mathbf{b})$. When each b_i is a real number in the interval $(0,1]$, then the effective measurement noise covariance matrix corresponding to eqn. (4.23) is $\mathbf{R}_{\mathbf{b}} = \sum_{i=1}^{m}\left(\frac{\sigma_i}{b_i}\right)^2 \mathbf{e}_i\mathbf{e}_i^{\top}$. The i-th measurement is progressively de-weighted as b_i is decreased from one toward zero. As b_i approaches zero, the effective covariance $(\sigma_i/b_i)^2$ approaches infinity, and the estimation effectively ignores the measurement y_i.

Chapter 5

Methods to Accommodate Outliers

This chapter presents two methods for accommodating outliers in state estimation.

5.1 Threshold Decisions

The traditional approach to detect and remove outliers in state estimation is based on a threshold test:

$$b_i \doteq \begin{cases} 0, & \text{when } |r_i| \geq \lambda \sigma_{r_i} \\ 1, & \text{when } |r_i| < \lambda \sigma_{r_i} \end{cases} \tag{5.1}$$

where $\lambda > 0$ is the decision parameter, $\sigma_{r_i}^2 = \mathbf{h}_i \mathbf{P} \mathbf{h}_i^\top + \sigma_i^2$ is the covariance of residual component r_i (see e.g.: [16, 17, 77]). The residual and predicted measurement are computed as

$$\mathbf{r} \doteq \mathbf{y} - \hat{\mathbf{y}} \quad \text{and} \quad \hat{\mathbf{y}} \doteq \mathbf{H} \hat{\mathbf{x}}^-. \tag{5.2}$$

The optimal estimate $\hat{\mathbf{x}}_{\mathbf{b}}$ and its posterior information $\mathbf{J}_{\mathbf{b}}^{+}$ are the solutions of eqn. (4.21) and eqn. (4.22).

This threshold test requires the designer to select a decision threshold λ. This choice trades-off *missed detections* relative to *false alarms*. When λ is so large that all measurements are included, the posterior information reaches its maximum. However, this inclusion strategy works well only in scenarios where outliers are absent. When outliers are present, a large λ results in a high probability of missed detections. The presence of outliers complicates the matter significantly. Consistency between the state estimate and its error covariance matrix is maintained only if outliers are completely eliminated at each epoch. Certainty of excluding outliers requires λ to be very small, which yields a high probability of false alarms. In practical applications, no outlier detection method is infallible. False alarms result in lost information. Since the TD approach uses a fixed value for λ that does not change to achieve a given performance specification, any such performance specification could be violated. Missed detection results in a corrupted state estimate mean $\hat{\mathbf{x}}_k^{+}$ and an overconfident covariance matrix, thus creating inconsistency between the actual and estimated uncertainty. This inconsistency renders subsequent outlier decisions unreliable.

5.2 RAPS Estimation using Diagonal Constraint

RAPS estimation finds an optimal (i.e., minimum risk) subset of measurements to achieve a state estimation accuracy specification (see [28, 29]). The specification on the solution is achieved by placing a constraint on the posterior information matrix in an optimization framework. The idea that a constraint only on the diagonal of the posterior information matrix (i.e., DiagRAPS) might allow an efficient computation of the solution is suggested in Section V-A of [29], but a computationally efficient solution to that idea has never been developed. It is now considered herein.

The DiagRAPS optimization problem [78, 79] is written as:

$$\left.\begin{aligned} \hat{\mathbf{x}}, \mathbf{b} &= \underset{\mathbf{x},\mathbf{b}}{\operatorname{argmin}}\, C(\mathbf{x},\mathbf{b}) \\ \text{s.t.:}\ \operatorname{diag}(\mathbf{J}_b^+) &\geq \mathbf{J}_l \end{aligned}\right\} \tag{5.3}$$

where the cost $C(\mathbf{x},\mathbf{b})$ is defined in eqn. (4.23). DiagRAPS optimizes over both the choice of measurements to include (i.e., $\mathbf{b}$) and the state estimate (i.e., $\mathbf{x}$). DiagRAPS interprets the cost $C(\mathbf{x},\mathbf{b})$ as the risk associated with the choice of measurements dictated by $\mathbf{b}$. This interpretation is based on the cost function having two terms. The first term quantifies how well the optimal estimate matches the prior. The second term quantifies the size of each measurement residual relative to the covariance $\mathbf{R}$, which is related to the risk of including each residual in the optimization.

The optimization is subject to a performance constraint. Because the information matrix arises naturally in the MAP solution (see eqn. (4.24)), the performance constraint is stated using information form, rather than covariance form, with $\mathbf{J}_l \in \mathbb{R}^n$ being a user-defined non-negative vector of minimum accuracy specifications.

Appendix A defines $\mathbf{G} \in \mathbb{R}^{n \times m}$ and $\mathbf{d} \in \mathbb{R}^n$ such that optimization problem (5.3) can be reformulated into more convenient problems.

5.2.0.1 Binary vector b

Optimization problem (5.3) can be rewritten as

$$\left.\begin{aligned} \hat{\mathbf{x}}, \mathbf{b} =& \operatorname*{argmin}_{\mathbf{x},\mathbf{b}} \|\mathbf{x}-\hat{\mathbf{x}}^-\|^2_{\mathbf{P}^-} + \sum_{i=1}^{m} \frac{b_i}{\sigma_i^2}(y_i - \mathbf{h}_i\mathbf{x})^2 \\ & \text{s.t.: } \mathbf{G}\,\mathbf{b} \geq \mathbf{d} \\ & \quad b_i \in \{0, 1\} \text{ for } i = 1, \ldots m. \end{aligned}\right\} \tag{5.4}$$

Both the objective function and the constraint are linear in **b**. The objective function is quadratic in **x**.

5.2.0.2 Non-binary vector b

Optimization problem (5.3) can be written as

$$\left.\begin{aligned} \hat{\mathbf{x}}, \mathbf{b} =& \operatorname*{argmin}_{\mathbf{x},\mathbf{b}} \|\mathbf{x}-\hat{\mathbf{x}}^-\|^2_{\mathbf{P}^-} + \sum_{i=1}^{m} \frac{b_i}{\sigma_i^2}(y_i - \mathbf{h}_i\mathbf{x})^2 \\ & \text{s.t.: } \mathbf{G}\,\mathbf{b} \geq \mathbf{d} \\ & \quad b_i \in [0, 1] \text{ for } i = 1, \ldots m. \end{aligned}\right\} \tag{5.5}$$

Both the objective function and the constraint are linear in **b**. The objective function is quadratic in **x**.

Note that Problem (5.5) differs from Problem (5.4) due to the domain of **b**.

Chapter 6

Solutions to DiagRAPS

This chapter presents computationally efficient approaches to solve the DiagRAPS optimization problems discussed in Sec. 5.2. Solutions for the binary or non-binary cases of **b** using the BCD method are proposed in Sections 6.1 and 6.2, respectively. Discussion of the convergence, optimality, and computational cost are presented in Sections. 6.3 and 6.4.

This section only discusses the solution for the DiagRAPS problems that have feasible solutions. There may be situations where no feasible solutions exist, meaning that there is insufficient information in the complete set of measurements to achieve the performance constraint. Sec. 6.5 presents a soft-constraint relaxation approach to address these situations.

6.1 Binary Solution

Problem (5.4) is a multi-convex mixed-integer nonlinear programming problem where the objective function is convex with respect to **x** and **b** individually, but not in combination. Using the BCD method [80, 81], the minimization of the cost $C(\mathbf{x},\mathbf{b})$ given in eqn. (4.23) constrained by the linear inequalities in Problem (5.4) can be solved by a two part iteration. The inputs to the algorithm include $\mathbf{H}$, $\mathbf{y}$, $\hat{\mathbf{x}}^-$, $\mathbf{P}^-$, and $\mathbf{R}$. The algorithm is initialized with $\ell = 0$ with $\mathbf{x}^0 = \hat{\mathbf{x}}^-$.

1. Select b for a fixed x: To start this step, the iteration counter is incremented: $\ell = \ell + 1$. During this step, $\mathbf{x}$ is held constant with value $\mathbf{x}^{\ell-1}$ and $C(\mathbf{x}^{\ell-1}, \mathbf{b})$ is minimized with respect to $\mathbf{b}$. Because the first term of $C(\mathbf{x}^{\ell-1}, \mathbf{b})$ is independent of $\mathbf{b}$, the effective optimization problem is

$$\left.\begin{aligned} \min : C(\mathbf{b} : \mathbf{x}^{\ell-1}) &= \sum_{i=1}^{m} \frac{b_i}{\sigma_i^2} (\mathbf{h}_i \mathbf{x}^{\ell-1} - y_i)^2 \\ \text{s.t.: } \mathbf{G}\,\mathbf{b} &\geq \mathbf{d} \\ b_i &\in \{0,\, 1\} \text{ for } i = 1, \ldots m. \end{aligned}\right\} \tag{6.1}$$

Problem (6.1) is a standard ILP problem. Assuming that a feasible solution exists, the result of this step is $\mathbf{b}^\ell$ with cost $C(\mathbf{x}^{\ell-1}, \mathbf{b}^\ell)$.

2. Select x for fixed b: In this step, the cost function $C(\mathbf{x}, \mathbf{b})|_{\mathbf{b}=\mathbf{b}^\ell}$ defined in eqn. (5.4) is minimized with respect to $\mathbf{x}$. This is an unconstrained optimization because of the constraint of eqn. (5.4) does not depend on $\mathbf{x}$. With $\mathbf{b} = \mathbf{b}^\ell$ being known, eqn. (4.19) and eqn. (4.21) compute $\hat{\mathbf{x}}^\ell = \hat{\mathbf{x}}_{\mathbf{b}^\ell}$, which achieves cost $C(\hat{\mathbf{x}}^\ell, \mathbf{b}^\ell)$.

The iteration is stopped when $C(\hat{\mathbf{x}}^\ell, \mathbf{b}^\ell) = C(\hat{\mathbf{x}}^{\ell-1}, \mathbf{b}^{\ell-1})$, which must occurs because the number of feasible b vectors is finite and $\hat{\mathbf{x}}$ of a given $\mathbf{b}$ is unique.

6.2 Non-binary Solution

When $\mathbf{b}$ is treated as a real variable, DiagRAPS estimation is defined by Problem (5.5). Applying the BCD method to Problem (5.5) yields a two-part iteration:

1. Select b for a fixed x: $\mathbf{b}^\ell$ is determined by solving the LP problem:

$$\left.\begin{aligned} \min: C(\mathbf{b}:\mathbf{x}^{\ell-1}) &= \sum_{i=1}^{m} \frac{b_i}{\sigma_i^2}(\mathbf{h}_i\mathbf{x}^{\ell-1} - y_i)^2 \\ \text{s.t.: } \mathbf{G}\,\mathbf{b} &\geq \mathbf{d} \\ b_i \in [0,\,1] &\text{ for } i = 1, \ldots m. \end{aligned}\right\} \tag{6.2}$$

2. Select x for fixed b: $\hat{\mathbf{x}}^\ell = \hat{\mathbf{x}}_{\mathbf{b}^\ell}$ by minimizing cost $C(\hat{\mathbf{x}}^\ell, \mathbf{b}^\ell)$ using eqn. (4.21) with $\mathbf{b} = \mathbf{b}^\ell$.

This non-binary approach provides a non-binary vector **b** to deactivate or de-weight the measurements. The resulting LP can be solved more efficiently than ILP, offering a potentially more robust and computationally tractable approach compared to the binary solution.

6.3 Convergence and Optimality

The following points provide insights into the optimality and convergence characteristics of the algorithm:

- Step 1 focuses on selecting a set of measurements to minimize the risk subject to a performance constraint.
- Step 1 of iteration $\ell = 1$ establishes an initial cost $C(\mathbf{x}^0, \mathbf{b}^1)$. After that point, each subsequent minimization step of each iteration results in decreasing cost:

$$C(\mathbf{x}^0, \mathbf{b}^1) \geq C(\mathbf{x}^1, \mathbf{b}^1) \geq C(\mathbf{x}^1, \mathbf{b}^2) \geq \cdots. \tag{6.3}$$

Since the cost is strictly positive and decreasing, this implies that the iteration will ultimately achieve the stopping condition, as long as there is at least one feasible solution.

- The BCD approach, as applied to both binary and non-binary solutions, converges to a local optimum of the DiagRAPS optimization problem. Appendix C demonstrates that Problem (5.4) can be reformulated as a convex programming problem. The comparative analysis of performance in the choice between the global or local optimization approaches are discussed in Sections 6.4 and 7.4.

6.4 Computation Cost

6.4.1 Locally Optimal Solution

For the non-binary solution, solving the LP problem as defined in Problem (6.2) is associated with polynomial-time complexity [82, 83]. In contrast, the binary solution for Problem (6.1) involves an ILP problem, which is an NP-hard problem. Although the worst-case scenario for solving an ILP problem has exponential-time complexity, ILP is well-investigated with several tools available for effectively solving it (e.g., 'intlinprog‘ in MATLAB, Google OR-Tools, SciPy Optimize). Common strategies for solving ILP/Mixed-ILP include LP relaxation, cut generation, and Branch & Bound algorithm, which collectively contribute to a polynomial-time average computational cost [84–87].

6.4.2 Globally Optimal Solution

For the binary problem, earlier work has suggested a depth-first search (DFS) strategy to exhaustively explore all possible combinations of binary vector **b** [29, 88] to find the global optimum. This exhaustive approach using DFS demands either permutation time complexity $O(m!)$ to examine all permutations of $\mathbf{b}$, including duplicates, or $O(2^m)$ time complexity and $O(2^m)$ space complexity to avoid duplicates. These solutions become increasingly impractical computationally as m increases. Although a convex programming formulation of Problem (5.4) is derived in Appendix C, it remains a mixed-integer nonlinear programming problem, introducing additional $n \times m$ variables. Solving this convex problem via CVX MOSEK requires the combination of a continuous optimization algorithm and an exhaustive search of the binary variables in $\mathbf{b}$ [88], which can lead to a time complexity of $O(2^m)$.

While solving the convex formulation for a global optimum of Problem (C.6) or (C.8) is possible, there are significant trade-offs to consider between the local and global solutions. Specifically for the GNSS applications discussed in this article, the CVX MOSEK toolbox requires tens of seconds to several minutes to resolve the convex programming problem for a single GNSS epoch, rendering it impractical for real-time applications. Experiment results and further discussions are provided in Sec. 7.4.

6.5 Performance Feasibility and Soft Constraint

The DiagRAPS optimization problem is solvable only when the performance constrain ($\mathbf{Gb} \geq \mathbf{d}$) is feasible. However, in certain conditions, such as the SAE specification discussed in Sec. 7.2, satisfying the constraint may not be possible even when all measurements are enabled ($\mathbf{b} = \mathbf{1}$), rendering the DiagRAPS optimization problem infeasible. To address this feasibility issue, this paper adopts a soft constraint approach using a vector of positive slack variables $\boldsymbol{\mu} = [\mu_1, ..., \mu_n]^\top$.

For the local optimum approach to solve Problem (5.4), the revised objective function is formulated as

$$C_\mu(\mathbf{x},\mathbf{b},\boldsymbol{\mu}) = \|\mathbf{x}-\hat{\mathbf{x}}^-\|^2_{\mathbf{P}^-} + \sum_{i=1}^{m} \frac{b_i}{\sigma_i^2}(y_i - \mathbf{h}_i\mathbf{x})^2 + \gamma\sum_{j=1}^{n}\boldsymbol{\mu} \tag{6.4}$$

where $\gamma\sum_{j=1}^{n}\boldsymbol{\mu}$ is the soft constraint penalty term and γ is a scaling parameter that determines the penalty's influence. The optimization problem, as originally stated in Problem (6.1), is then reformulated to a Mixed-ILP problem that accommodates the relaxed constraints:

$$\left.\begin{aligned} &\min : C_\mu(\mathbf{b},\boldsymbol{\mu} : \mathbf{x}^{\ell-1}) = \\ &\qquad \sum_{i=1}^{m}\frac{b_i}{\sigma_i^2}(\mathbf{h}_i\mathbf{x}^{\ell-1} - y_i)^2 + \gamma\sum_{j=1}^{n}\boldsymbol{\mu} \\ &\text{s.t.: } \mathbf{g}_j\mathbf{b} + \mu_j \geq d_j - L_j, \\ &\qquad \mu_j \in \begin{cases} [0, L_j], & \mathbf{g}_j\mathbf{1} > d_j \\ [0, \mathbf{g}_j\mathbf{1}], & \mathbf{g}_j\mathbf{1} \leq d_j \end{cases} \text{for } j = 1, \ldots n, \\ &\qquad b_i \in \{0, 1\} \text{ for } i = 1, \ldots m. \end{aligned}\right\} \tag{6.5}$$

where $L_j = max(d_j - \mathbf{g}_j\mathbf{1}, 0)$, $\mathbf{g}_j$ is the j-th row of $\mathbf{G}$, $d_j = \mathbf{J}_l(j) - \mathbf{J}_d^-(j)$ is the j-th element of $\mathbf{d}$, and $\mathbf{J}_l(j)$ and $\mathbf{J}_d^-(j)$ represent the j-th element of $\mathbf{J}_l$ and $\mathbf{J}_d$, respectively.

Problem (6.5) considers two conditions. First, when the performance specification constraints are feasible the maximum diagonal information that can be achieved for the j-th state is greater than the specification:

$$\mathbf{g}_j\mathbf{1} + \mathbf{J}_d^-(j) > \mathbf{J}_l(j) \Rightarrow \mathbf{g}_j\mathbf{1} > d_j.$$

Therefore, $L_j = 0$ and $\mu_j = 0$. In this situation, Problem (6.5) is equivalent to the original Problem (6.1). Second, when either the performance constraints is infeasible (i.e., $\mathbf{g}_j\mathbf{1} < d_j$) or all measurements are required to be selected (i.e., $\mathbf{g}_j\mathbf{1} = d_j$), $L_j = d_j - \mathbf{g}_j\mathbf{1}$, which is positive. The constraint in Problem (6.5) is then

$$\begin{aligned} &\mathbf{g}_j\mathbf{b} + \mu_j \geq d_j - L_j \\ \Rightarrow\ &\mathbf{g}_j\mathbf{b} + \mu_j \geq \mathbf{g}_j\mathbf{1} \\ \Rightarrow\ &\mathbf{g}_j\mathbf{b} + \mathbf{J}_d^-(j) + \mu_j \geq \mathbf{g}_j\mathbf{1} + \mathbf{J}_d^-(j) \end{aligned}$$

where $\mathbf{g}_j\mathbf{b} + \mathbf{J}_d^-(j)$ is the posterior information of the j-th state for a given $\mathbf{b}$, $\mathbf{g}_j\mathbf{1} + \mathbf{J}_d^-(j)$ is the maximum achievable posterior information, and μ_j represents the reduction of information relative to the maximum achievable information to balance the risk relative to the feasibility. Therefore, μ_j ranges from $\mathbf{g}_j\mathbf{0}$ to $\mathbf{g}_j\mathbf{1}$ (i.e., $\mu_j \in [0, \mathbf{g}_j\mathbf{1}]$).

The convex formulation for the globally optimal approach in the binary case is presented as Problem (C.8) in Appendix C. Problem (6.2) in the non-binary solution can be relaxed with soft constraints similar to Problem (6.5), where the objective function is still $C_\mu(\mathbf{b}, \boldsymbol{\mu} : \mathbf{x}^{\ell-1})$ with $\mathbf{b}$ being non-binary.

This relaxation requires the designer to specify a value for γ. For the GNSS applications employed in this article, the choice of γ is discussed in Sec. 7.2.

Chapter 7

Experimental Evaluation

7.1 Data Description

The experimental evaluation focuses on demonstrating the efficacy of DiagRAPS compared to traditional approaches. Both the DGNSS and PPP approaches are evaluated. The VN-DGNSS approach utilizes equivalent information to PPP but provides the correction pattern differently. As it requires the receiver's native solution, this chapter does not concentrate on DiagRAPS in VN-DGNSS applications. The experiment implementation code can be found in `https://github.com/Azurehappen/GNSS-Risk-Averse-Estimation`.

7.1.1 DGNSS Data

The open-source University of Texas Challenge for Urban Positioning (TEX-CUP) dataset is utilized for the experimental evaluation in DGNSS applications [**?**]. The evaluation encompasses a multi-GNSS application, incorporating signals from GPS L1, GLONASS L1, GALILEO E1, and Beidou B1. The elevation cut-off is 10 degrees. These GNSS measurements were collected using two Septentrio receivers (one for the rover and one for the base) to enable DGNSS applications. For the purpose of evaluation, the dataset also provides a ground truth trajectory. During the experiment, the vehicle route traverses the west campus of The University of Texas at Austin and downtown Austin. This route includes portions with a challenging environment containing viaducts, tall buildings, large structures and trees. It is a hard-urban area that is prone to frequent and significant outlier measurements. Visual depictions of the street views are available in Fig. 5 of [**?**]. When the vehicle traverses the urban area with narrow lanes and tall buildings surrounding, the GNSS signal may experience serve multipath and non-line-of-sight errors for any satellite. This dataset spans approximately 1.5 hours, encompassing about 5000 epochs with one-second measurement intervals (i.e., $T = 1$).

7.1.2 PPP Data

This experimental evaluation focuses on GNSS positioning using DiagRAPS and RT-PPP corrections. To be comparable with automotive applications, a low-cost u-blox F9P receiver is used to acquire the raw GNSS measurements on a moving platform. The analysis of multi-GNSS RT-PPP is performed using GPS L1, Galileo E1, and Beidou B1 signals. The elevation cut-off is 10 degrees. The experimental vehicle navigated through urban and residential zones near University of California-Riverside (UCR), traversing areas characterized by narrow lanes lined with tall trees, under a relatively clear view of the sky. Throughout the experiment, the u-blox maintained communication with a nearby base station. The $ground\ truth$ trajectory was established using u-blox's native multi-GNSS, dual-frequency, integer-fixed RTK solution to achieve centimeter accuracy. This dataset spans approximately 20 minutes, encompassing about 1300 epochs with one-second measurement intervals.

7.2 Performance Specification and Feasibility

The SAE J2945 specification stipulates accuracy requirements for highway vehicle applications, requiring horizontal accuracy to be better than 1.5 m and vertical accuracy better than 3 m, both at 68% probability. The computation of the performance constraint parameter $\mathbf{J}_l$ to achieve the SAE J2945 specification is described in Section III-B of [29]. The optimization problem performance constraint is applied only for the position and velocity variables, by defining $\mathbf{J}_l = [\mathbf{J}_p^\top, \mathbf{J}_v^\top]^\top$ with

$$\mathbf{J}_p = [1.389, 1.389, 0.347]^\top \text{ and } \mathbf{J}_v = [2.778, 2.778, 0.694]^\top.$$

The first two elements of $\mathbf{J}_p$ and $\mathbf{J}_v$ specify the local tangent plane north and east direction information bounds, while the third elements are that of vertical direction.

The SAE J2945 standard applies for open sky conditions. However, the primary focus of this experiment is on challenging scenarios, such as hard urban environments, where the availability and quality of satellite signals is often compromised. Therefore, the optimization formulas discussed in Sec. 6.5 are used to perform the experimental analysis.

This relaxation requires the designer to specify a value for γ. When the prior $\mathbf{x}^-$ is reliable, each measurement residual term (i.e., $(\mathbf{h}_i \mathbf{x} - y_i)^2/\sigma_i^2$) typically remains below 10 in GNSS applications. However, in areas with significant outliers, the value of this term could rise above 100. The optimization strategy employed in Problem (6.5) is intended to selecting measurements with lower residuals, indicative of lower risk, and discarding those with excessively high values. Choosing an appropriate value for γ is crucial. If γ is too small, the optimization favors larger values of $\boldsymbol{\mu}$ minimizing the objective function at the expense of using fewer or no measurements (losing information). Conversely, a very large γ results in the selection of all measurements, regardless of their risk. For the analysis conducted in this experiment, γ is set to 50. This value is chosen to balance the trade-off between rejecting measurements with high risks and retaining a sufficient value to satisfy the performance specification.

7.3 Metrics

Roadway applications typically focus on horizontal positioning accuracy. Vertical positioning accuracy are included for reference. The cost function defined in eqn. (4.23) quantifies the risk for all states in $\mathbf{x}$ and is dimensionless. Metrics are thus established as follows:

- North, East and Down (NED) frame coordinate errors: δp_N, δp_E, δp_D;
- Posterior error covariance of the position in NED frame: σ_N^2, σ_E^2, σ_D^2;
- Horizontal positioning error: $HE = \sqrt{\delta p_N^2 + \delta p_E^2}$;
- Vertical positioning error: $VE = |\delta p_D|$;
- Horizontal estimation error Standard Deviation (STD): $HorSTD = \sqrt{\sigma_N^2 + \sigma_E^2}$;
- Vertical estimation error STD: $VerSTD = \sqrt{\sigma_D^2}$;
- For the binary case, the optimal objective value is quantified by $C_\mu(\mathbf{x}_k^+, \mathbf{b}, \boldsymbol{\mu})$ as defined in eqn. (6.4) or $C_g(\mathbf{x}_k^+, \mathbf{b}, \mathbf{q}, \boldsymbol{\mu})$ as defined in eqn. (C.7). In the experimental results, C_μ represents the local optimal objective value obtained from the BCD method, while C_g denotes the global optimal objective value solved by CVX MOSEK;
- Estimation risk as quantified by $C(\mathbf{x}_k^+, \mathbf{b})$ as defined in eqn. (4.23);
- DiagRAPS penalty term: $\gamma \sum_{j=1}^{n} \boldsymbol{\mu}$;

The metrics intentionally include actual errors (e.g., δp_N, δp_E, δp_D) and theoretical characterization of those errors (e.g., σ_N^2, σ_E^2, σ_D^2). This enables comparison of how the estimator is actually doing with how the theory predicts that it is doing.

7.4 Comparison of DiagRAPS Optimization Methods

Before comparing the binary and non-binary cases presented in Chapter. 6, it is useful to compare the global or local approach for the binary case. Two approaches to solve the DiagRAPS for the binary case, as discussed in Sec. 6.3,

Evaluating the entire dataset for the globally optimal approach is impractical, due to its runtime. Therefore, this comparison focuses on a subset containing 200 one-second epochs of TEX-CUP driving data. The runtime for the globally optimal approach for this subset took about 2 hours. The experiment results were processed using MATLAB on an AMD 5800x processor.

7.4.1 Global versus Local Optimization

To accurately assess how close the locally optimal approach is to the globally optimal approach, it is crucial to compare results computed from exactly equivalent objective functions and parameter values. To achieve this, in this subsection only, both solutions utilize the same values of $\mathbf{x}^-$, $\mathbf{P}^-$, $\mathbf{y}$, $\mathbf{H}$, and $\mathbf{R}$ at each epoch. Starting from these same settings, each approach converges to its optimal posterior state: $\mathbf{x}^+$ and $\mathbf{P}^+$. After convergence, we record and evaluate the optimal objective value and computation time using for each approach separately; then, only the globally optimal posterior state is used for time propagation.

Fig. 7.1 illustrates the comparison of optimality between the two solutions. Subplot (a) shows the objective values of the globally optimal solution in blue and of the locally optimal solution in red. Subplot (b) presents the difference in optimal objective value (i.e., $C_\mu - C_g$). These graphs show that the global optimum approach always achieves a lower optimal objective value as expected. The gap between the globally optimal and locally optimal solutions is generally narrow.

Subplot (c) displays the computation time at each epoch for those two solutions. The computation time for the globally optimal approach ranges from a few seconds to several minutes per epoch, rendering it infeasible for real-time applications. In contrast, the locally optimal approach has computation time per epoch that is typically less than 0.1 seconds, which is significantly more efficient than the globally optimal approach.

7.4.2 State Estimation Performance

To analyze and compare the overall and actual state estimation performance, we independently (i.e., each approach used its own posterior state in the time propagation) processed the 200-second data subset data using each approach. Because each approach delivers different posterior information at the initial epoch, their optimization problems are distinct at all subsequent times, having different values for $\mathbf{G}$, $\mathbf{d}$, and $\mathbf{P}^-$. Therefore, they are not directly comparable epoch-by-epoch. The non-binary DiagRAPS results are included for comparison. Fig. 7.2 presents the comparison of the cumulative probability distribution of horizontal positioning errors, vertical positioning errors, and estimation risk, leading to the following observations:

Subplot a and b: The global and local optimization approaches for binary DiagRAPS offer similar positioning accuracy. Non-binary DiagRAPS has slightly better performance in the horizontal accuracy. Specifically, for horizontal positioning performance, 96.00% of positioning errors were less than 1.5 meters for the local optimum binary approach, compared to 98.00% for the global optimum binary approach and 98.50% for the non-binary approach. For vertical positioning performance, 97.50% of positioning errors were less than 3 meters for the local optimum approach, compared to 97.00% for the global optimum approach and 97.00% for the non-binary approach.

Subplot c: All approaches yield comparable estimation risks. The globally optimal approach does offer higher probability at the lower level of risk levels. But the difference between them is not notable.

7.4.3 Summary

This subsection has highlighted the trade-offs between the optimality of the solution and the computational efficiency required for real-time applications. While the globally optimal approach provides the best solution for a given objective function, the locally optimal approach offers a very similar solution at significantly lower computational cost. The performance difference between globally optimal binary approach and non-binary approach are not significant. Therefore, for the case of binary **b**, only the locally optimal solution method is used for the subsequent DiagRAPS performance evaluation.

7.5 Estimators

The performance evaluation of DiagRAPS estimation is conducted using four distinct estimators. These estimators use identical time propagation procedures; however, their measurement update processes differ.

Kalman Filter (KF): Determines the posterior state $\mathbf{x}^+$ by minimizing the cost function as defined in eqn. (4.23) utilizing all measurements (i.e., $\mathbf{b} = \mathbf{1}$).

TD: Selects $\mathbf{b}$ based on the threshold test in eqn. (5.1) with $\lambda = 2$. It then determines the posterior state $\mathbf{x}^+$ by minimizing the cost function as defined in eqn. (4.23).

RAPS-bi: Uses DiagRAPS to choose binary $\mathbf{b}$ to minimize the cost function in eqn. (6.4). The binary $\mathbf{b}$ determines which measurements are used.

RAPS-nb: Uses DiagRAPS to choose non-binary $\mathbf{b}$ to minimize the cost function in eqn. (6.4) The non-binary $\mathbf{b}$ determines the measurement de-weighting.

The evaluation of these estimators focuses on their risk and the statistical analysis of positioning errors, examining key aspects.

7.6 Evaluation in DGNSS Applications

This section compares the performance of DiagRAPS with traditional estimation methods in the DGNSS approach, utilizing the entirety of the DGNSS dataset.

7.6.1 Overall Performance Across the Four Estimators

Fig. 7.3a plots the risk versus time for the four estimation approaches. This graph highlights that DiagRAPS, both in its binary and non-binary forms, consistently achieves lower risk in over 98% of epochs compared to KF and TD. This superior performance is particularly evident during vehicular movement in urban areas that is characterized by frequent and severe GNSS multipath (i.e., $k \in [500, 4500]$). In contrast, during stationary phases or in open-sky environments (i.e., $k \leq 500$ or $k > 4500$), the difference in estimation risk among the methods is less pronounced. Fig. 7.3(b) show the values of the penalty term in the soft constraint approaches. A zero value in this penalty term indicates that the performance specification constraint is being met. A non-zero value means the constraint is not feasible. Fig. 7.3(c) shows the number of measurements excluded at each epoch (i.e, for the non-binary case, the i-th measurement is considered as excluded when $b_i \leq 0.01$.) No green graph is presented in this subplot as the KF uses all measurements. The purple graph shows the total number of measurements available. Although both binary and non-binary DiagRAPS have similar risk profiles and penalty term values, certain epochs, such as around the 3000th epoch, show noticeable differences between the two. These differences underscore the flexibility advantage of non-binary DiagRAPS. Unlike the binary approach, which can only select or reject measurements outright, non-binary DiagRAPS has more flexibility to trade-off between constraint satisfaction and cost minimization by de-weighting measurements.

In many epochs, the risk of the KF and TD are sufficiently similar that the KF graphs are covered by the TD graphs in the visual representations. The yellow graphs in Fig. 7.3(c) reveal that most measurement residuals satisfy the TD test, even with the relatively small decision threshold $\lambda = 2.0$. There are several epochs where KF exhibits significantly higher risk compared to TD,

Table 7.1: Horizontal position error statistics.

Methods	Mean (m)	RMS (m)	Max (m)	Prob. of HE ≤ 1.0 m	Prob. of HE ≤ 1.5 m
EKF	6.33	11.55	103.42	42.45%	47.47%
TD	4.44	**7.84**	103.42	43.65%	49.32%
RAPS-bi	5.84	12.82	69.83	57.38%	63.90%
RAPS-nb	**4.23**	9.73	**56.22**	**60.22%**	**67.97%**

Table 7.2: Vertical position error statistics.

Methods	Mean (m)	RMS (m)	Max (m)	Prob. of VE ≤ 3.0 m
EKF	15.24	26.04	123.57	43.52%
TD	11.00	**18.08**	**100.52**	45.29%
RAPS-bi	9.49	22.26	147.85	65.52%
RAPS-nb	**7.51**	18.88	131.93	**68.59%**

demonstrating TD's ability to effectively reject severe outliers. In contrast, DiagRAPS adopts a different approach, selecting a subset of measurements that optimally minimizes the risk when performance specifications are achievable or, alternatively, minimizing the cost using a soft constraint when strict adherence to the performance specification is not feasible. In such cases, when the soft constraint penalty term is non-zero, the estimator is aware that the specification is not being met and can alert the maneuver planner for the application so that the application can adjust accordingly. The KF and TD approaches cannot do the same due to the fact that their covariance is wrong (i.e., inconsistent) due to the inclusion of outlier measurements.

Tables 7.1 and 7.2 display statistics for each estimator for various of the metrics defined in Section 7.3 for the horizontal and vertical positioning. The best results in each category is highlighted in bold.

Non-binary DiagRAPS achieves the lowest mean in positioning errors, while TD demonstrates the lowest RMS error. All estimators record significant maximum errors, attributable to severe outlier conditions encountered in the challenging portions of the experiment.

Fig. 7.4 presents the cumulative probability distribution for horizontal (subplot (a)) and vertical (subplot (b)) positioning errors. The legend defines a color coding for each estimator that is consistent with Fig. 7.3. The cumulative probability distribution graphs elucidate the superior performance of both DiagRAPS approaches, showing that they achieve probability of achieving smaller errors. Specifically, non-binary DiagRAPS outperforms other methods, with approximately 68% probability of maintaining horizontal errors below 1.5 m and vertical errors below 3 m. This level of performance in this challenging urban environment even meets the SAE specifications which are defined for open sky conditions, underscoring the efficacy of the non-binary DiagRAPS approach in challenging environments.

Fig. 7.5 is a scatter plot showing the horizontal positioning error on the *y*-axis and predicted posterior error STD (i.e., the square root of the norm of the appropriate diagonal elements of $\mathbf{P}^{+}$) on the *x*-axis, using the same color scheme as in Fig. 7.3 for KF, TD, RAPS-bi, and RAPS-nb. The left plot displays the horizontal positioning error. The right plot presents the vertical positioning error. The black line in each plot represents the *line-of-consistency* along which the actual positioning performance equals the predicted estimation accuracy. Consequently, the plots are divided into two distinct regions:

1. **Over-confident region:** The region above the line-of-consistency represents a risky and unsafe estimation scenario. In this region the estimator is overconfident because its actual

Table 7.3: Percentage of results in the conservative region.

	KF	TD	RAPS-bi	RAPS-nb
Horizontal	42.43%	44.06%	70.00%	75.16%
Vertical	13.03%	13.77%	67.17%	69.37%

estimation error is greater than the estimators theoretical characterization of its estimation error.

2. **Conservative region:** The region above the line-of-consistency represents a conservative estimation scenario. In this region, the estimator achieves an actual accuracy that is better than it predicts.

Table 7.3 summarizes the percentage of results from Fig. 7.5 in the conservative regions for each estimator. Non-binary DiagRAPS achieves the highest performance, securing 75.16% and 69.37% of points in the conservative regions for horizontal and vertical cases, respectively. The DiagRAPS approaches demonstrate an approximate advantage of 30% and 50% in conservative performance over the other methods. These statistics indicate that KF and TD tend to produce more over confident estimates. For example in Region 1, the KF and TD predict accuracy with a STD of 0.8-1.5 meters, while the actual positioning errors often exceed 2-10 meters. In contrast, the Region 1 points from DiagRAPS are generally closer to the line-of-consistency, suggesting that the DiagRAPS does a better job of characterizing the accuracy that it is achieving.

7.6.2 Binary versus Non-binary RAPS

The preceding sections have established that DiagRAPS is both better able to achieve a given specification and better able to predict its accuracy in challenging measurement conditions.

Table 7.4: Position error probabilities for binary and non-binary DiagRAPS under feasibility and infeasible conditions.

		HE $\leq$ 1.0 m	HE $\leq$ 1.5 m	VE $\leq$ 3.0 m
Feasible Constraint	RAPS-bi	89.49%	94.57%	92.66%
	RAPS-nb	90.82%	96.05%	95.47%
Soft Constraint	RAPS-bi	39.64%	46.95%	50.53%
	RAPS-nb	45.95%	54.88%	52.14%

This section focuses on differentiating between binary and non-binary DiagRAPS in terms of their performance under different feasibility conditions.

Fig. 7.6 (a) and (b) show the DiagRAPS the DiagRAPS cumulative probability distributions of the positioning errors for horizontal and vertical results, respectively, for epochs that are feasible. Subplots (c) and (d) display results for epochs that are infeasible and therefore employ soft constraints. Notably, feasible constraint conditions typically coincide with scenarios where the vehicle experiences a relatively clear view of the sky. In contrast, soft constraints are necessitated in more challenging environments where insufficient measurements are available to meet the performance specifications. The proportion of epochs with feasible constraints is 35.59% for binary DiagRAPS and 31.78% for non-binary DiagRAPS. The graphs show that the binary and non-binary DiagRAPS perform similarly when the constraints are feasible. Non-binary DiagRAPS exhibits superior horizontal positioning performance in more challenging environments where soft constraints are applied.

Table 7.4 summarizes the probability metrics for this comparison, showing that non-binary DiagRAPS outperforms binary DiagRAPS across all metrics. Under feasible performance specification constraints, both binary and non-binary DiagRAPS exceed SAE specifications with comparable performance. However, when the problem is infeasible and soft constraints are required, non-binary DiagRAPS demonstrates an approximate 7% advantage in horizontal probability metrics. This advantage can be attributed to the ability of non-binary DiagRAPS to select more measurements with diverse weightings to minimize cost, thereby offering enhanced robustness.

7.6.3 DiagRAPS Computation Time

Fig. 7.7 displays a histogram of the per epoch computation time for binary and non-binary DiagRAPS. The computation time for KF and TD is typically less than 0.01 seconds, as these methods do not involve optimization. Both binary and non-binary DiagRAPS maintain computation times typically less than 0.06 seconds. Non-binary DiagRAPS achieves faster computation times compared to binary DiagRAPS, attributed to the less complex LP problem it solves, which can be processed more efficiently than the Mixed-ILP problem in binary DiagRAPS.

7.7 Evaluation in RT-PPP Applications

This sections compares the performance of DiagRAPS with traditional estimation methods in the RT-PPP approach, utilizing the entirety of the PPP dataset. Section 7.6 has demonstrated that non-binary DiagRAPS yields the best overall performance and lower computation costs compared to binary DiagRAPS. Hence, this section primarily focuses on the results from non-binary DiagRAPS.

The performance of the three estimators is evaluated based on their estimation risk and positioning accuracy. The subplot a in Fig. 7.8 display the risks across all epochs. The red graph indicates that DiagRAPS consistently achieves the lowest risk. Both KF and TD exhibit risks that are significantly higher than that of DiagRAPS. In many epochs, the risk difference between KF and TD is small, so the KF data is covered by the TD data. This shows that for most time epochs, most residuals passed the TD test, even with the reasonable small value of λ. Notably, during specific epochs (around 600s and 1000s), KF demonstrates a pronounced risk, whereas TD exhibits a reduced risk due to its ability to reject severe outliers.

The subplot b in Fig. 7.8 display the number of measurements discarded by DiagRAPS or TD. DiagRAPS selects a subset of measurements to minimize risk while achieving the performance specifications. The solution is feasible for all epochs, even while removing many more measurements than TD. At each epoch, DiagRAPS adapts both the number of satellites removed and the specific satellites removed based on the number and geometry of the available measurements as well as their specific residuals. This selection results in the reduced risk demonstrated in the top figure while achieving the performance specification.

Fig. 7.9 presents the cumulative probability distribution for both horizontal and vertical positioning errors, using a consistent color scheme with Fig. 7.8. Tables 7.5 and 7.6 provide a summary of statistics for each estimator for the horizontal and vertical positioning, including the mean, RMS, maximum horizontal and vertical errors, and the probability of the positioning errors being less than the specified threshold corresponding to the SAE specification. The best results in each category is highlighted in bold.

Throughout the entire experimental period, DiagRAPS consistently delivers superior results, except for the probability of vertical errors being less than 3 meters, which is 3.84% lower than that of TD. However, DiagRAPS exhibits the lowest mean, RMS, and maximum errors in vertical statistics, while KF and TD result in a high percentage of severe errors, as shown in subplot b of Fig. 7.9. Additionally, DiagRAPS showed a higher probability for vertical errors being less

Table 7.5: Horizontal position error statistics for PPP experiment.

Methods	Mean (m)	RMS (m)	Max (m)	Prob. of HE $\leq$ 1.0 m	Prob. of HE $\leq$ 1.5 m
EKF	0.94	1.65	12.72	74.88%	86.13%
TD	0.77	1.00	4.72	76.55%	88.19%
RAPS-nb	**0.70**	**0.86**	**3.84**	**77.34%**	**93.42%**

Table 7.6: Vertical position error statistics for PPP experiment.

Methods	Mean (m)	RMS (m)	Max (m)	Prob. of VE $\leq$ 3.0 m
EKF	1.72	2.81	20.01	84.63%
TD	1.54	2.18	11.17	**87.00%**
RAPS-nb	**1.46**	**1.99**	**6.23**	83.52%

than 1.5 meters. For horizontal errors less than 1.5 meters, DiagRAPS demonstrates an advantage of 7.29% over KF and 5.23% over TD. SF RT-PPP performance of these three estimators all surpass the SAE requirements.

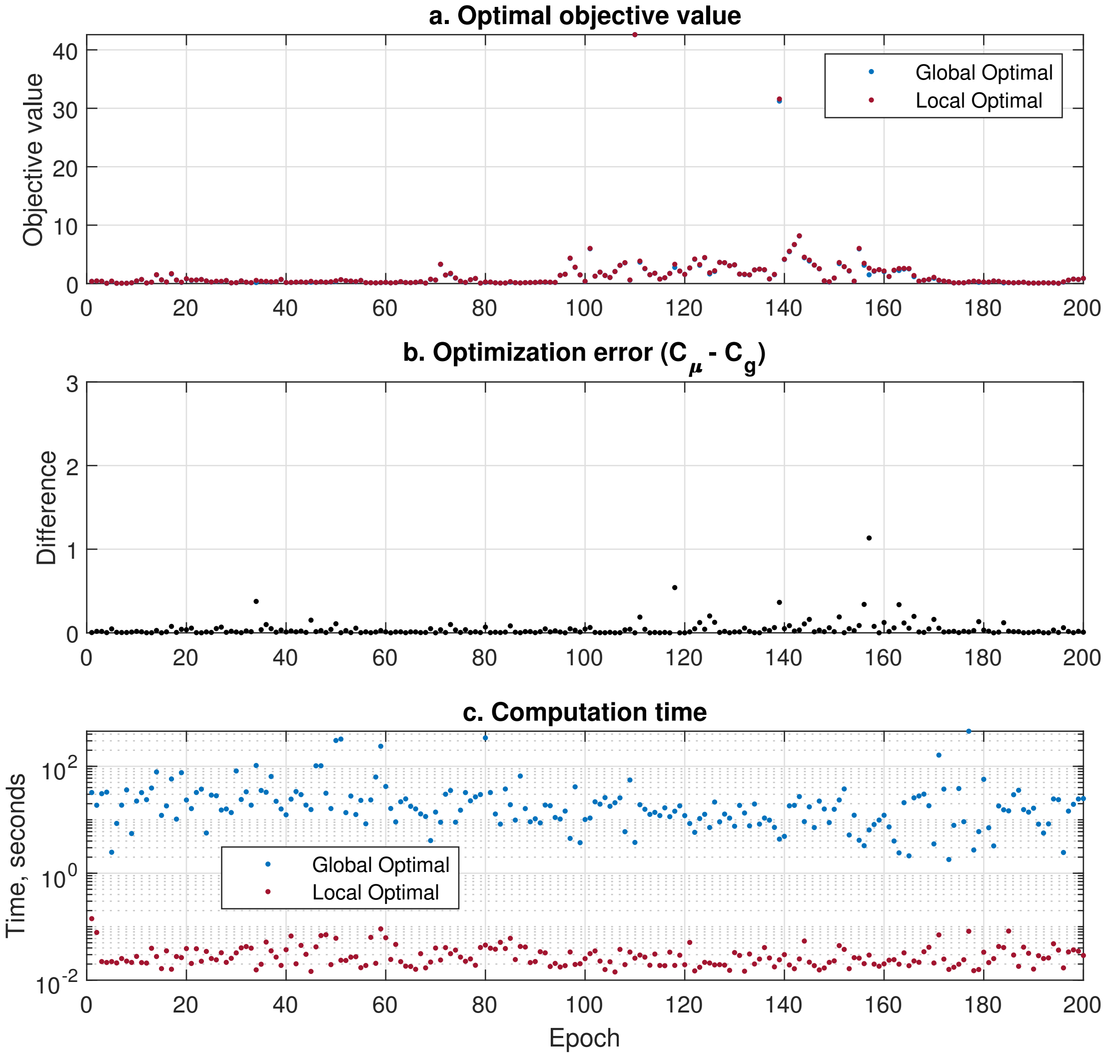

Figure 7.1: Comparison of optimality between the globally and locally optimal approaches. Results were derived using the same set of coefficients for the objective function at each epoch. Subplot (a) shows the optimal objective values obtained by each approach. Subplot (b) shows the difference between the objective values obtained by each approach. Subplot (c) shows the computation time in seconds required to solve the optimization problem at each epoch.

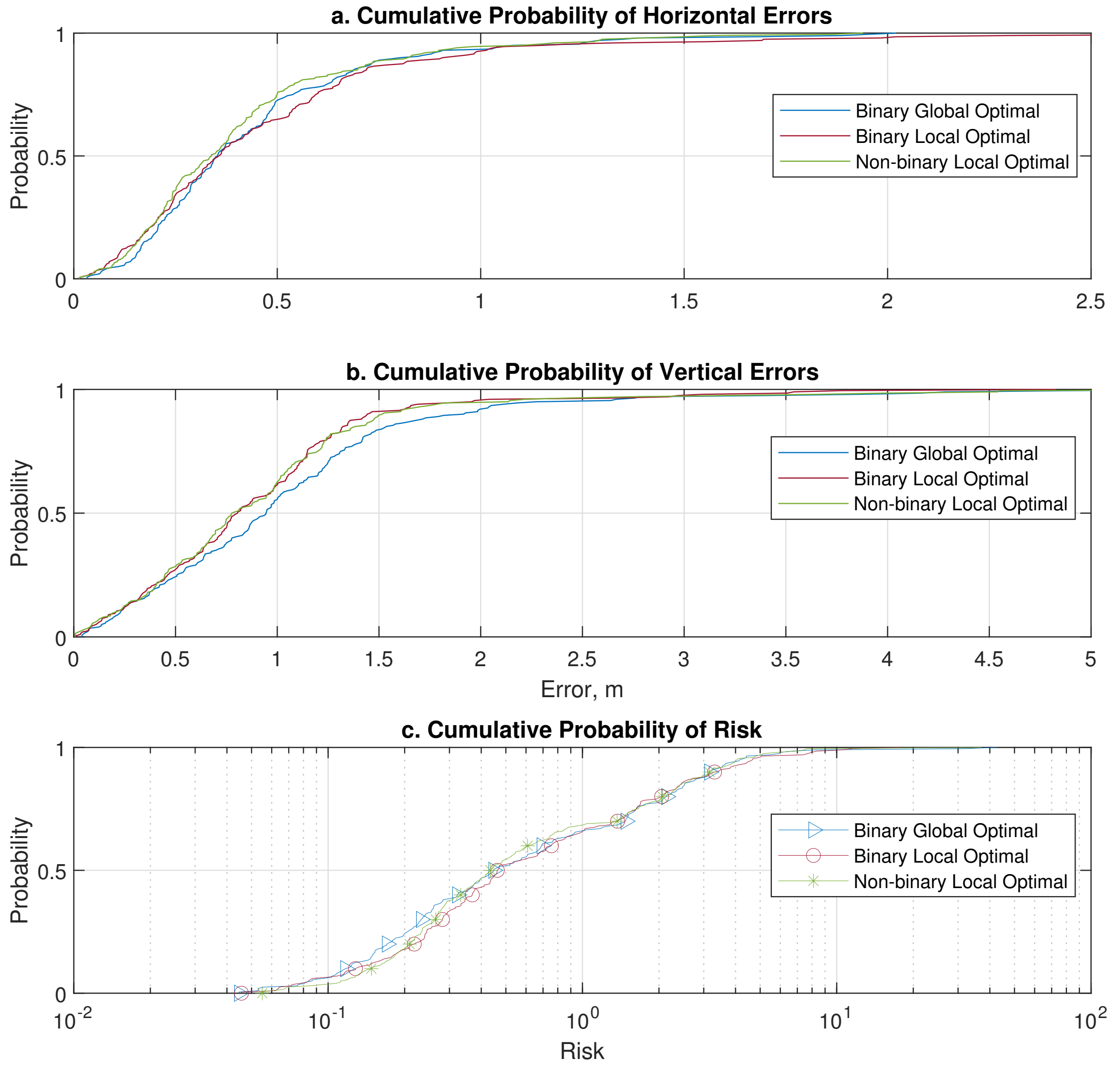

Figure 7.2: Cumulative probability curves for DiagRAPS using the globally and locally optimal approaches for the binary case and the locally optimal approach for the non-binary case. The blue and red curves shows the globally and locally optimal binary DiagRAPS results, respectively; and, the green curve shows the non-binary DiagRAPS results. Subplot (a) shows the cumulative probability of the horizontal positioning errors. Subplot (b) shows the cumulative probability of the horizontal positioning errors. Subplot (c) shows the cumulative probability of the optimal objective values (i.e., Risk).

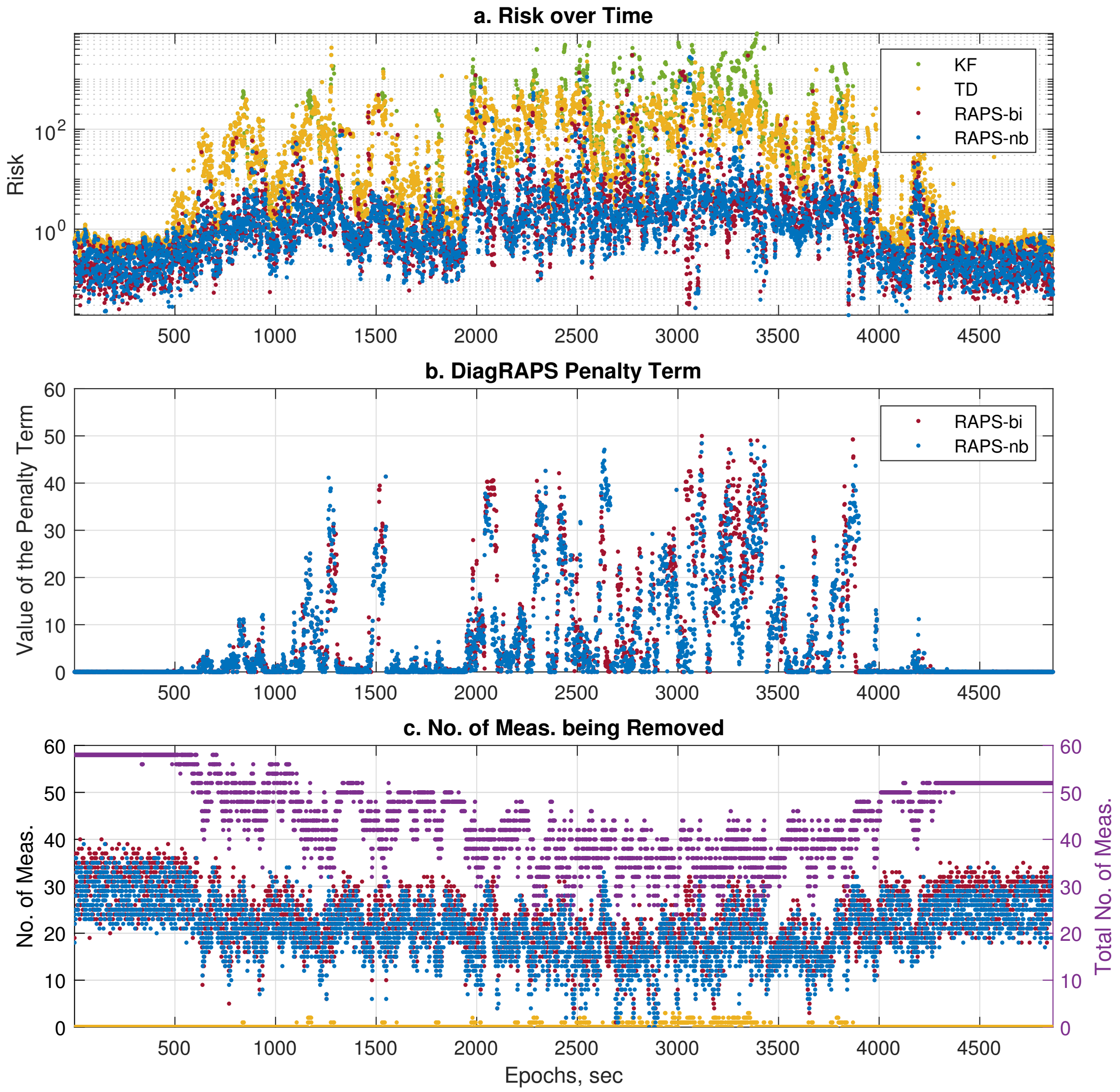

Figure 7.3: (a) Estimation risk for each epoch (KF is green, TD is yellow, RAPS-bi is red, RAPS-nb is blue). (b) Soft constraint penalty term values of binary and non-binary DiagRAPS as defined in eqn. (6.4). (c) Number of measurements excluded by TD, RAPS-bi, and RAPS-nb. Graph colors are as described for Subplot (a). The purple graph shows the total number of measurements available in each epoch.

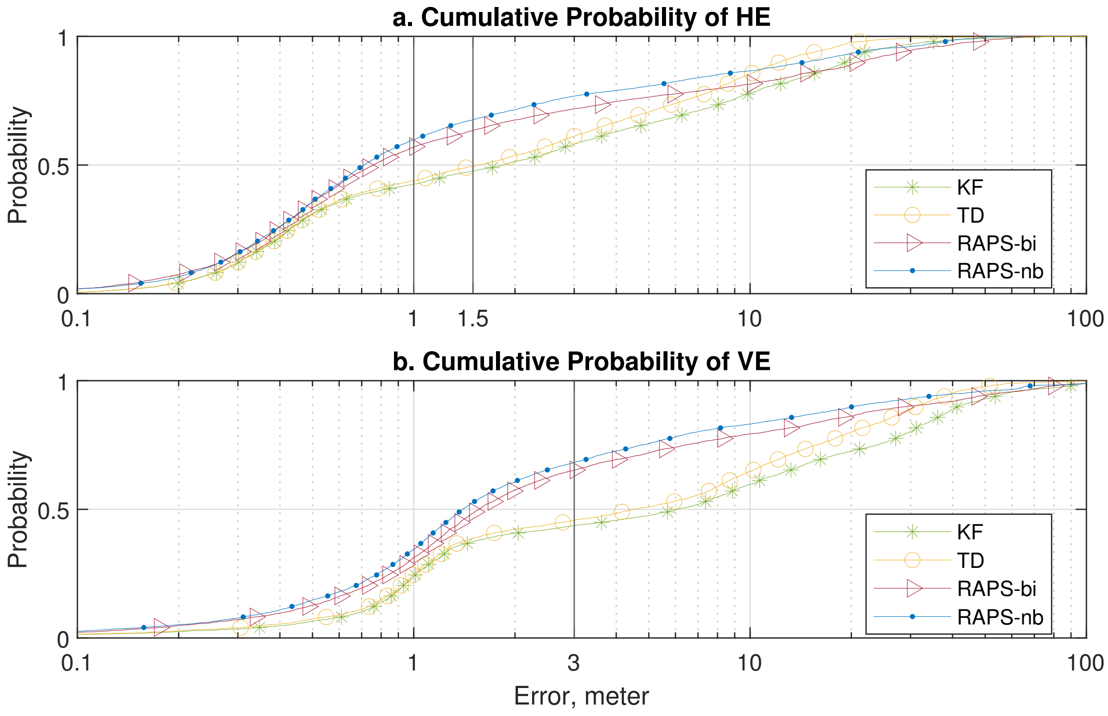

Figure 7.4: Cumulative distribution of horizontal (subplot (a)) and vertical (subplot (b)) position errors for the four estimators defined in Section 7.5.

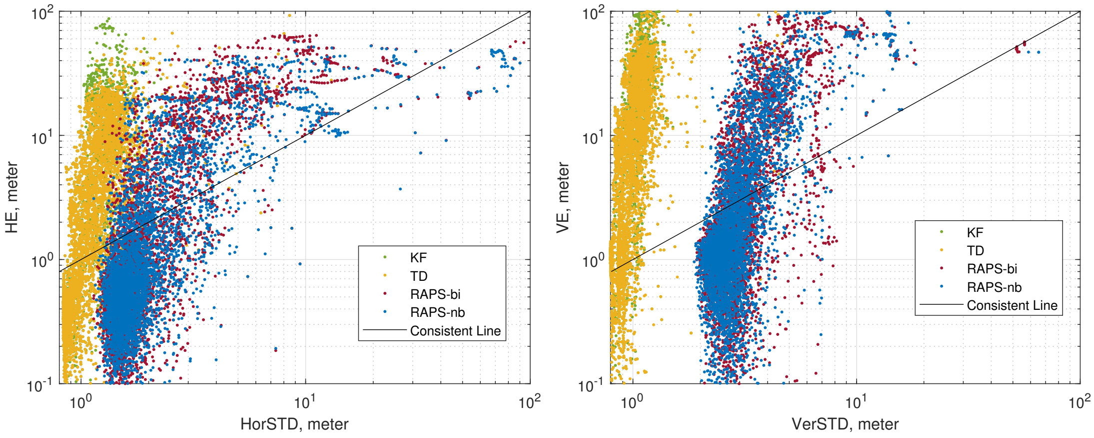

Figure 7.5: Positioning errors versus their STD. The left (right) plot shows actual horizontal (vertical) positioning error versus the posterior error standard deviation predicted by the estimator. The black line represents the line-of-consistency. The color scheme used is consistent with Fig. 7.3.

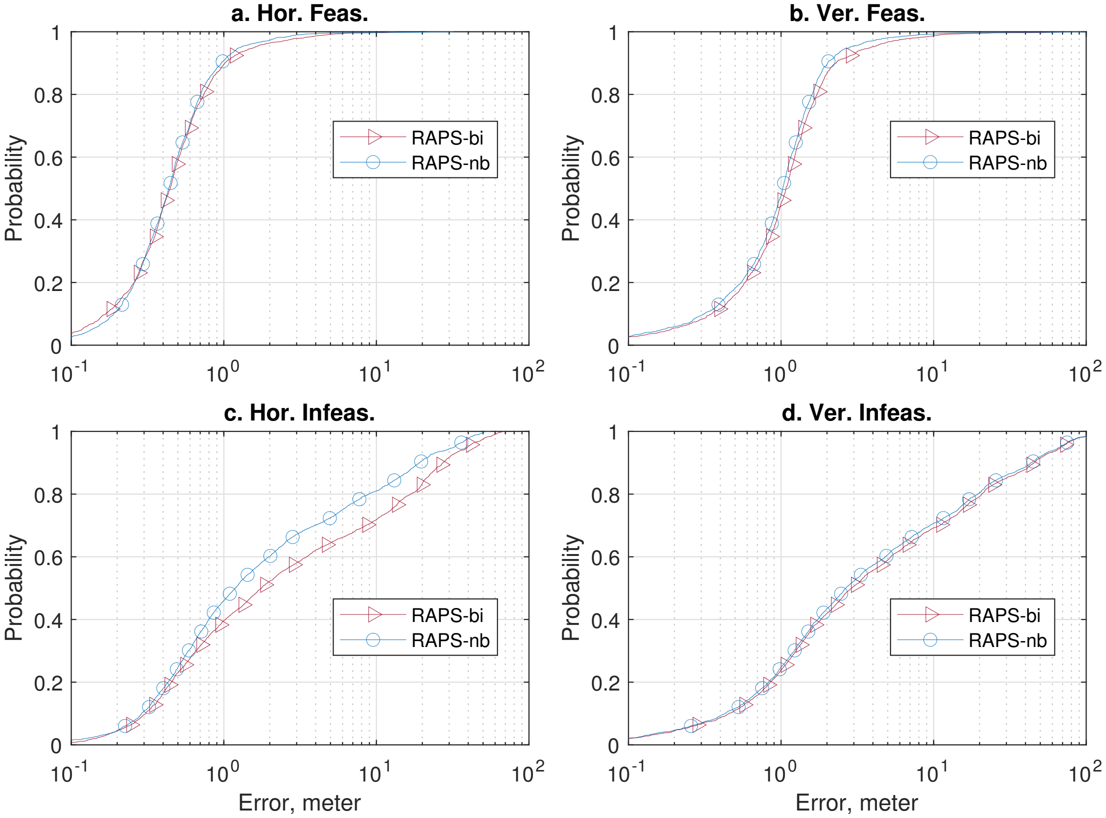

Figure 7.6: Cumulative position error distribution for binary DiagRAPS (red) and non-binary DiagRAPS (blue). Subplots (a) and (b) present horizontal and vertical results from epochs with feasible constraints, while subplots (c) and (d) display results from epochs employing soft constraints.

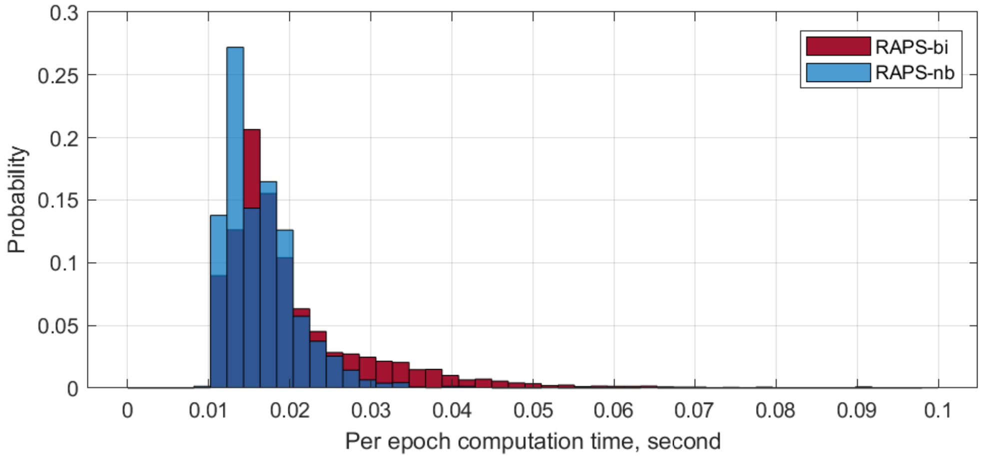

Figure 7.7: Probability histogram of the per epoch computation time for binary and non-binary DiagRAPS. The red bars represent binary DiagRAPS, and the blue bars represent non-binary DiagRAPS. In areas of overlap, the dark blue color highlights the shorter bar.

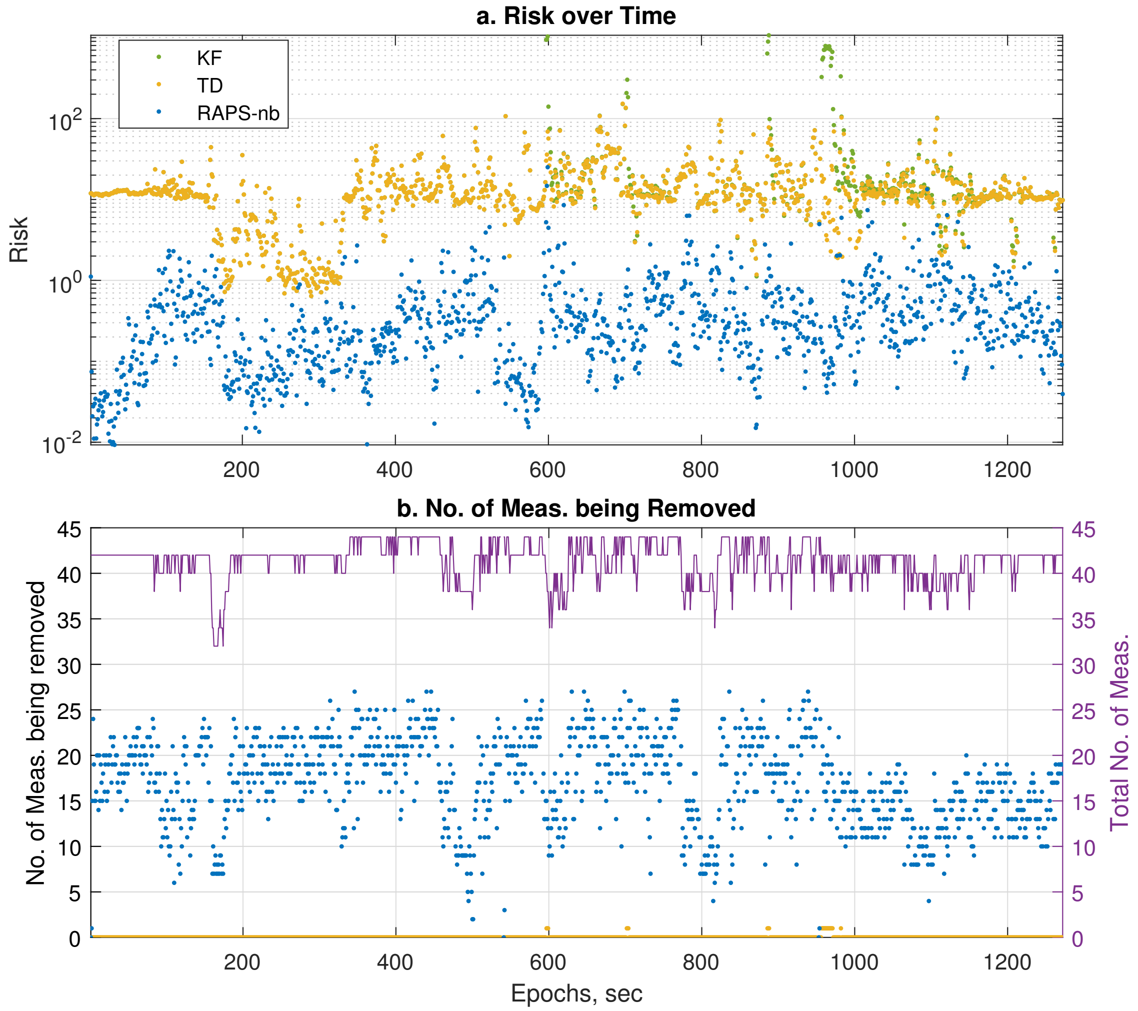

Figure 7.8: (a) Experimental results for the risk from KF in green, TD in yellow, and non-binary DiagRAPS in blue. (b) The number of measurements removed by either DiagRAPS or TD (left *y*-axis) and the total number of measurements available (right *y*-axis). The number of measurements available is equivalent to the number used by the KF.

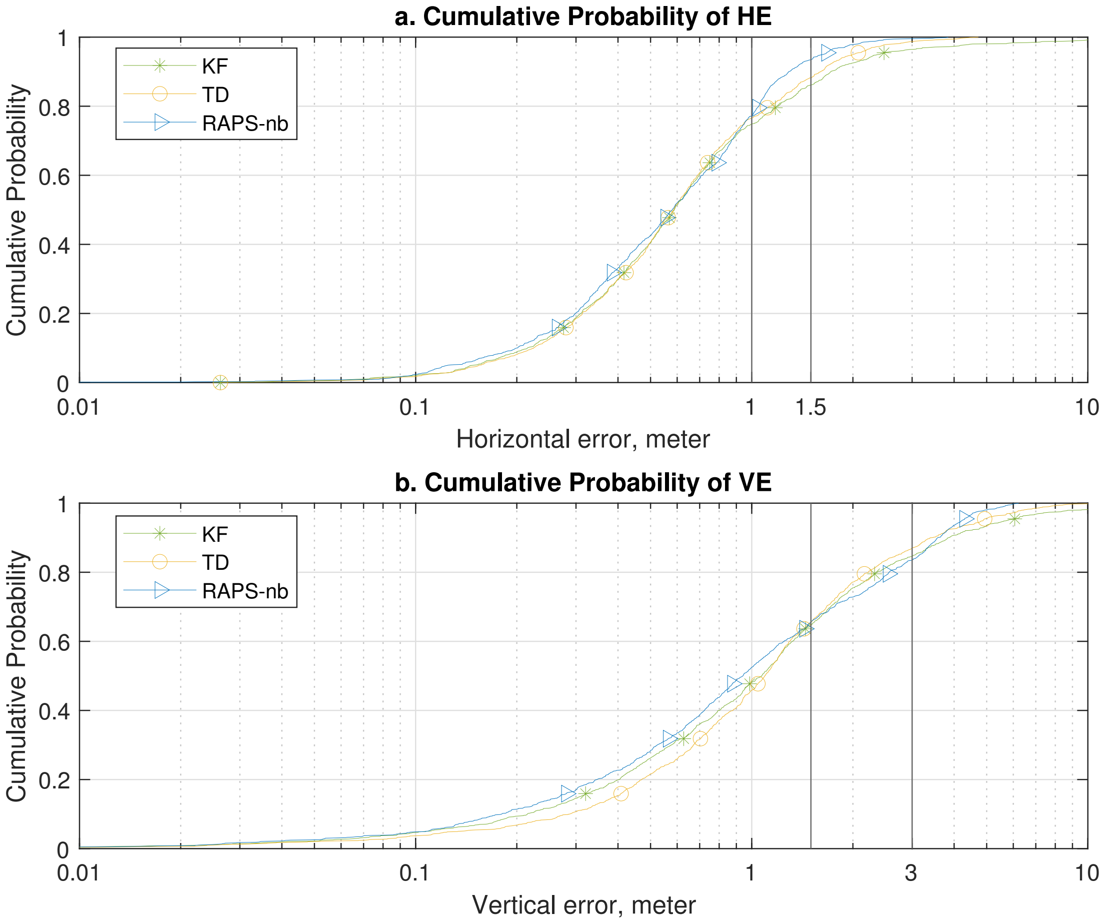

Figure 7.9: The cumulative error distribution of horizontal (a) and vertical (b) positioning errors for KF in green, TD in yellow, and DiagRAPS in blue for the entire experiment trajectory.

Chapter 8

Conclusion and Future Research Ideas

This article first reviewed two major GNSS pseudorange error mitigation approaches: DGNSS and RT-PPP, detailing their models and discussing correction sources. It then presented and validated two computationally efficient approaches for solving the risk-averse linear state estimation problem with a diagonal performance specification (i.e., DiagRAPS). These methods, leveraging BCD for both binary and non-binary measurement selection variables, ensure locally optimal solutions. The binary DiagRAPS focuses on selecting or rejecting measurements, while non-binary DiagRAPS offers a flexible approach by weighting measurements.

The DiagRAPS optimization problem for binary measurement selection has been reformulated into a convex programming problem, solvable by existing tools that guarantee a globally optimal solution. For applications where time is not a critical factor, this globally optimal approach provides the best solution for binary DiagRAPS. For the application of interest herein, the BCD approach provides results very similar to the global optimum, with a significantly lower computational cost, making it suitable for real-time applications.

This study also introduced relaxed formulations of DiagRAPS with soft constraints to accommodate situations where the specified performance was infeasible with the available measurements. This approach allows DiagRAPS to balance the risk of outlier inclusion relative to sacrificing feasibility. When this occurs, DiagRAPS is able to communicate the lack of feasibility to the application-level planner so that it can adjust the application behavior appropriately.

The experimental evaluation conducted multi-GNSS SF applications using both DGNSS and PPP approaches. For DGNSS, real-world driving data from hard urban environments was used, while for PPP, the data was collected under relatively clear sky conditions. RT-PPP corrections, applicable globally without the need for local base stations, overcome the limitations of DGNSS. In the DGNSS evaluation, the performance of both binary and non-binary DiagRAPS approaches was assessed and compared to solutions using all measurements in a KF and a traditional outlier rejection approach based on normalized residual magnitudes. The results showed that binary and non-binary DiagRAPS offered an advantage of at least 14% in horizontal and 20% in vertical SAE probability metrics compared to KF and TD, as detailed in the rightmost columns of Tables 7.1 and 7.2. Notably, the non-binary approach had the lowest computation cost and the best overall performance. In the PPP evaluation, KF, traditional TD, and non-binary DiagRAPS were evaluated and compared. The results indicated that all approaches exceeded SAE specifications when employing PPP techniques for real-time applications. Particularly in challenging scenarios with obscured sky views and heightened multipath effects, the DiagRAPS approach demonstrated its efficacy in decreasing outlier effects, leading to less severe positioning errors. Overall, DiagRAPS showed improvements of 5.23% over TD and 7.29% over KF in horizontal positioning performance, with comparable results in vertical performance according to Fig. 7.9, Tables 7.5 and 7.6.

Several avenues for future research are interesting. First, this article concentrated on diagonal performance specifications due to the linear constraints that facilitate computationally efficient solutions and the ease of incorporating soft constraints when no feasible solutions exist. For computation-insensitive applications, incorporating the full performance specification (i.e., $\mathbf{J}_b^+ \geq \mathbf{J}_l$) could yield more robust results, as the joint information could become significant. However, properly applying soft constraints to RAPS estimations dominated by semi-definite programming problems presents a greater challenge. Second, enhanced positioning accuracy could be achieved by incorporating RTK with GNSS carrier phase measurements. This extension would necessitate a double-difference operation on the carrier phase measurements, resulting in a non-diagonal measurement noise matrix (i.e., $\mathbf{R}$). Therefore, investigating RAPS estimation for non-diagonal $\mathbf{R}$ matrices presents an intriguing opportunity. While diagonalizing $\mathbf{R}$ is straightforward, this method distributes outlier effects across multiple transformed measurements. Additionally, in PPP applications, incorporating carrier-phase measurements aligns with the PPP RTK technique. Leveraging carrier-phase measurements in an SF context presents challenges. This direction becomes more viable with the anticipated launch of the third stage of the SSR schedule by IGS in the near future [10]. Extending the DiagRAPS approach to multi-frequency applications within PPP is also intriguing. Significant ionospheric error sources can be substantially mitigated through measurement combinations. Third, urban areas often lack a sufficient number of outlier-free GNSS signals to meet SAE specifications. In these cases, sensor fusion techniques incorporating a broader array of sensors (e.g., Inertial Measurement Unit (IMU), camera-aided systems, lidar) could be advantageous. Developing such extensions would necessitate further advancements in DiagRAPS methods for non-linear systems.

Bibliography

[1] N. Williams and M. Barth, “A Qualitative Analysis of Vehicle Positioning Requirements for Connected Vehicle Applications,” *IEEE Intell. Transp. Syst. Mag.*, vol. 13, no. 1, pp. 225–242, 2020.

[2] K. Boriboonsomsin, M. J. Barth, W. Zhu, and A. Vu, “Eco-routing Navigation System Based on Multisource Historical and Real-time Traffic Information,” *IEEE Trans. Intell. Transp. Syst.*, vol. 13, no. 4, pp. 1694–1704, 2012.

[3] J. A. Farrell, G. Wu, W. Hu, D. Oswald, and P. Hao, “Lane-Level Localization and Map Matching for Advanced Connected and Automated Vehicle (CAV) Applications,” *National Center for Sustainable Transportation (NCST) (UTC)*, 2023. [Online]. Available: https://doi.org/10.7922/G25T3HSS

[4] V. Barnett and T. Lewis, *Outliers in Statistical Data*. Wiley, 1994.

[5] Anonymous, “On-Board System Requirements for V2V Safety Communications J2945/1_201603,” *Society of Automotive Engineers*, 2016.

[6] GPS Product Team, “Global Positioning System Standard Positioning Service Performance Analysis Report,” *GPS Product Team: Washington, DC, USA*, 2020. [Online]. Available: https://www.nstb.tc.faa.gov/reports/2020_Q4_SPS_PAN_v2.0.pdf

[7] Anonymous, “BeiDou Navigation Satellite System Open Service Performance Standard (Version 2.0),” *China Satellite Navigation Office*, 2018.

[8] J. A. Farrell, *Aided Navigation: GPS with High Rate Sensors*. McGraw-Hill, Inc., 2008.

[9] P. Teunissen and O. Montenbruck, *Springer handbook of global navigation satellite systems*. Springer, 2017.

[10] International GNSS Service, “IGS state space representation (SSR) format version 1.00,” *IGS Real-Time Working Group*, 2020. [Online]. Available: https://files.igs.org/pub/data/format/igs_ssr_v1.pdf

[11] F. O. Silva, W. Hu, and J. A. Farrell, “Real-Time Single-Frequency Precise Point Positioning for Connected Autonomous Vehicles: A Case Study Over Brazilian Territory,” in *22nd IFAC World Congress*, vol. 56, no. 2, 2023, pp. 5703–5710.

[12] W. Hu, A. Neupane, and J. A. Farrell, “Using PPP Information to Implement a Global Real-Time Virtual Network DGNSS Approach,” *IEEE Trans. Veh. Technol.*, vol. 71, no. 10, pp. 10 337–10 349, 2022.

[13] P. Misra and P. Enge, *Global Positioning System: Signals, Measurements and Performance Second Edition*. Ganga-Jamuna Press, 2006.

[14] L.-T. Hsu, S.-S. Jan, P. D. Groves, and N. Kubo, “Multipath Mitigation and NLOS Detection using Vector Tracking in Urban Environments,” *GPS Solutions*, vol. 19, pp. 249–262, 2015.

[15] A. S. Willsky, “A Survey of Design Methods for Failure Detection in Dynamic Systems,” *Automatica*, pp. 601–611, 1976.

[16] R. J. Patton and J. Chen, “A Review of Parity Space Approaches to Fault Diagnosis,” *IFAC Proceedings Volumes*, vol. 24, no. 6, pp. 65–81, 1991.

[17] P. M. Frank and X. Ding, “Survey of Robust Residual Generation and Evaluation Methods in Observer-Based Fault Detection Systems,” *J. of Process Control*, vol. 7, pp. 403–424, 1997.

[18] E. Navon and B.-Z. Bobrovsky, “An Efficient Outlier Rejection Technique for Kalman Filters,” *Signal Processing*, vol. 188, p. 108164, 2021.

[19] A. E. Beaton and J. W. Tukey, “The Fitting of Power Series, Meaning Polynomials, Illustrated on Band-Spectroscopic Data,” *Technometrics*, vol. 16, no. 2, pp. 147–185, 1974.

[20] P. J. Rousseeuw and K. Van Driessen, “Computing LTS Regression for Large Data Sets,” *Data Mining and Knowledge Discovery*, vol. 12, no. 1, pp. 29–45, 2006.

[21] R. A. Maronna, R. D. Martin, V. J. Yohai, and M. Salibián-Barrera, *Robust Statistics: Theory and Methods (with R)*. John Wiley & Sons, 2019.

[22] D. Wang, H. Lu, and M.-H. Yang, “Robust Visual Tracking via Least Soft-threshold Squares,” *IEEE Trans. Circuits Syst. Video Technol.*, vol. 26, no. 9, pp. 1709–1721, 2015.

[23] P. J. Rousseeuw and A. M. Leroy, *Robust Regression and Outlier Detection*. John Wiley & Sons, 2005.

[24] P. J. Rousseeuw, “Least Median of Squares Regression,” *J. of the American Statistical Association*, vol. 79, no. 388, pp. 871–880, 1984.

[25] N. Sünderhauf and P. Protzel, “Switchable Constraints vs. Max-Mixture Models vs. RRR-A Comparison of Three Approaches to Robust Pose Graph SLAM,” in *2013 IEEE ICRA*. IEEE, 2013, pp. 5198–5203.

[26] J. Shi, H. Yang, and L. Carlone, “ROBIN: a Graph-Theoretic Approach to Reject Outliers in Robust Estimation using Invariants,” in *2021 IEEE ICRA*. IEEE, 2021, pp. 13 820–13 827.

[27] L. Carlone, A. Censi, and F. Dellaert, “Selecting Good Measurements via $\ell 1$ Relaxation: A Convex Approach for Robust Estimation over Graphs,” in *2014 IEEE/RSJ IROS*, 2014, pp. 2667–2674.

[28] E. Aghapour, F. Rahman, and J. A. Farrell, "Outlier Accommodation by Risk-Averse Performance-Specified Linear State Estimation," in *IEEE CDC*. IEEE, 2018, pp. 2310–2315.

[29] E. Aghapour, F. Rahman, and J. A. Farrell, "Outlier Accommodation in Nonlinear State Estimation: A Risk-Averse Performance-Specified Approach," *IEEE Trans. Control Syst. Technol.*, pp. 1–13, 2019.

[30] W. Song, W. Yi, Y. Lou, C. Shi, Y. Yao, Y. Liu, Y. Mao, and Y. Xiang, "Impact of GLONASS pseudorange inter-channel biases on satellite clock corrections," *GPS Solutions*, vol. 18, no. 3, pp. 323–333, 2014.

[31] L. Wanninger, "Carrier-phase inter-frequency biases of GLONASS receivers," *J. of Geodesy*, vol. 86, no. 2, pp. 139–148, 2012.

[32] M. J. Dunn, "Global Positioning Systems Directorate System Engineering & Integration Interface Specification IS-GPS-200H," *Navstar GPS Space Segment/Navigation User Interfaces*, 2013.

[33] Anonymous, "Galileo Signal in Space Interface Control Document (OS SIS ICD)," *Galileo Open Service*, 2008.

[34] ——, "BeiDou Navigation Satellite System Signal in Space Interface Control Document Open Service Signal B1I (Version 3.0)," *China Satellite Navigation Office*, 2019.

[35] B. Stressler, J. Heck, and H. Steve, "An assessment of the accuracy of broadcast ephemerides for multi-GNSS positioning," in *IGS workshop*, 2018.

[36] J. Geng, X. Chen, Y. Pan, and Q. Zhao, "A Modified Phase Clock/Bias Model to Improve PPP Ambiguity Resolution at Wuhan University," *J. of Geodesy*, vol. 93, no. 10, pp. 2053–2067, 2019.

[37] N. Wang, Y. Yuan, Z. Li, O. Montenbruck, and B. Tan, "Determination of differential code biases with multi-GNSS observations," *J. of Geodesy*, vol. 90, no. 3, pp. 209–228, 2016.

[38] O. Montenbruck, A. Hauschild, and P. Steigenberger, "Differential code bias estimation using multi-GNSS observations and global ionosphere maps," *J. of the Inst. of Navigation*, vol. 61, no. 3, pp. 191–201, 2014.

[39] O. Bock and E. Doerflinger, "Atmospheric Modeling in GPS Data Analysis for High Accuracy Positioning," *Physics and Chemistry of the Earth, Part A*, vol. 26, no. 6-8, pp. 373–383, 2001.

[40] W. Hu and J. A. Farrell, "Derivation of Earth-Rotation Correction (Sagnac) and Analysis of the Effect of Receiver Clock Bias," University of California, Tech. Rep., 2019. [Online]. Available: https://escholarship.org/uc/item/1bf6w7j5

[41] ——, "Derivation of the Earth-Rotation Correction (Sagnac Effect) and Analysis of its Accuracy for GNSS Applications," *Under Review*, 2024.

[42] F. Rahman, F. Silva, Z. Jiang, and J. A. Farrell, "ECEF Position Accuracy and reliability: Continent Scale Differential GNSS Approaches (Phase C Report)," *Technical Report: UC Riverside*, 2019. [Online]. Available: https://escholarship.org/uc/item/05p9p3c9

[43] D. Laurichesse, F. Mercier, and J.-P. Berthias, "Real-time PPP with Undifferenced Integer Ambiguity Resolution, Experimental Results," in *Proc. of the 23rd International Technical Meeting of The Satellite Division of the Institute of Navigation*, 2010, pp. 2534–2544.

[44] J. Zumberge, M. Heflin, D. Jefferson, M. Watkins, and F. Webb, "Precise Point Positioning for the Efficient and Robust Analysis of GPS Data from Large Networks," *J. of Geophysical Research: Solid Earth*, vol. 102, no. B3, pp. 5005–5017, 1997.

[45] T. Hadas and J. Bosy, "IGS RTS Precise Orbits and Clocks Verification and Quality Degradation over Time," *GPS Solutions*, vol. 19, no. 1, pp. 93–105, 2015.

[46] E. Sardon, A. Rius, and N. Zarraoa, "Estimation of the transmitter and receiver differential biases and the ionospheric total electron content from Global Positioning System observations," *Radio Science*, vol. 29, no. 03, pp. 577–586, 1994.

[47] J. Ray and K. Senior, "Geodetic techniques for time and frequency comparisons using GPS phase and code measurements," *Metrologia*, vol. 42, no. 4, p. 215, 2005.

[48] S. Schaer, "SINEX BIAS—Solution (Software/technique) independent exchange format for GNSS biases version 1.00," in *IGS Workshop on GNSS Biases, Bern, Switzerland*, 2016.

[49] N. Wang, Z. Li, B. Duan, U. Hugentobler, and L. Wang, "GPS and GLONASS observable-specific code bias estimation: comparison of solutions from the IGS and MGEX networks," *J. of Geodesy*, vol. 94, no. 8, pp. 1–15, 2020.

[50] R. Leandro, M. Santos, and R. Langley, "Unb neutral atmosphere models: development and performance," in *Proc. of the National Technical Meeting of The Institute of Navigation*, 2006, pp. 564–573.

[51] W. Li, Y. Yuan, J. Ou, H. Li, and Z. Li, "A new global zenith tropospheric delay model IGGtrop for GNSS applications," *Chinese Science Bulletin*, vol. 57, no. 17, pp. 2132–2139, 2012.

[52] K. Kazmierski, M. Santos, and J. Bosy, "Tropospheric Delay Modelling for the EGNOS Augmentation System," *Survey Review*, vol. 49, no. 357, pp. 399–407, 2017.

[53] N. Penna, A. Dodson, and W. Chen, "Assessment of EGNOS tropospheric correction model," *J. of Navigation*, vol. 54, pp. 37 – 55, 01 2001.

[54] W. Li, Y. Yuan, J. Ou, Y. Chai, Z. Li, Y.-A. Liou, and N. Wang, "New versions of the BDS/GNSS zenith tropospheric delay model IGGtrop," *J. of Geodesy*, vol. 89, no. 1, pp. 73–80, 2015.

[55] W. Li, Y. Yuan, J. Ou, and Y. He, "IGGtrop_SH and IGGtrop_rH: Two improved empirical tropospheric delay models based on vertical reduction functions," *IEEE Trans. Geosci. Remote Sens.*, vol. 56, no. 9, pp. 5276–5288, 2018.

[56] J. A. Klobuchar, "Ionospheric Time-Delay Algorithm for Single-Frequency GPS Users," *IEEE Trans. Aerosp. Electron. Syst.*, pp. 325–331, 1987.

[57] Anonymous, "Ionospheric Correction Algorithm for Galileo Single Frequency Users (V1.2)," *European GNSS Service Centre*, 2016.

[58] Y. Yuan, X. Huo, J. Ou, K. Zhang, Y. Chai, D. Wen, and R. Grenfell, "Refining the Klobuchar ionospheric coefficients based on GPS observations," *IEEE Trans. Aerosp. Electron. Syst.*, vol. 44, no. 4, pp. 1498–1510, 2008.

[59] A. Angrisano, S. Gaglione, C. Gioia, M. Massaro, and U. Robustelli, "Assessment of NeQuick Ionospheric Model for Galileo Single-Frequency Users," *Acta Geophysica*, vol. 61, no. 6, pp. 1457–1476, 2013.

[60] R. S. Committee *et al.*, "Proposal of new RTCM SSR messages, SSR stage 2: Vertical TEC (VTEC) for RTCM standard 10403.2 differential GNSS (Global Navigation Satellite Systems) services-version 3," *RTCM Special Committee*, 2014.

[61] Z. Li, N. Wang, M. Hernandez-Pajares, Y. Yuan, A. Krankowski, A. Liu, J. Zha, A. Garcia-Rigo, D. Roma-Dollase, H. Yang *et al.*, "IGS real-time service for global ionospheric total electron content modeling," *J. of Geodesy*, vol. 94, no. 3, pp. 1–16, 2020.

[62] Z. Li, Y. Yuan, N. Wang, M. Hernandez-Pajares, and X. Huo, "SHPTS: Towards a new method for generating precise global ionospheric TEC map based on spherical harmonic and generalized trigonometric series functions," *J. of Geodesy*, vol. 89, no. 4, pp. 331–345, 2015.

[63] D. Laurichesse and A. Blot, *New CNES real time products including BeiDou.* IGS Mail No. 7183, 10 Nov 2015.

[64] T. Fuller-Rowell, "USTEC: a new product from the space environment center characterizing the ionospheric total electron content," *GPS Solutions*, vol. 9, no. 3, pp. 236–239, 2005.

[65] M. B. El-Arini, P. A. O'Donnell, P. M. Kellam, J. A. Klobachar, T. C. Wisser, and P. H. Doherty, "The FAA wide area differential GPS (WADGPS) static ionospheric experiment," in *Proc. of the National Technical Meeting of the Institute of Navigation*, 1993, pp. 485–496.

[66] F. D. S. Prol, P. D. O. Camargo, and M. T. D. A. H. Muella, "Comparative study of methods for calculating ionospheric points and describing the GNSS signal path," *Boletim de Ciências Geodésicas*, vol. 23, no. 4, pp. 669–683, 2017.

[67] Z. Nie, H. Yang, P. Zhou, Y. Gao, and Z. Wang, "Quality Assessment of CNES Real-time Ionospheric Products," *GPS Solutions*, vol. 23, pp. 1–15, 2019.

[68] G. Weber, L. Mervart, and A. Stürze, *BKG Ntrip Client (BNC): Version 2.12.* Verlag des Bundesamtes für Kartographie und Geodäsie, 2016.

[69] T. Takasu and A. Yasuda, "Development of the low-cost RTK-GPS receiver with an open source program package RTKLIB," *Int. Symposium on GPS/GNSS*, vol. 1, 2009.

[70] G. Seeber, *Satellite geodesy.* Walter de gruyter, 2003.

[71] S. Khanafseh, B. Kujur, M. Joerger, T. Walter, S. Pullen, J. Blanch, K. Doherty, L. Norman, L. de Groot, and B. Pervan, "GNSS Multipath Error Modeling for Automotive Applications," in *Proc. of ION GNSS+*, 2018, pp. 1573–1589.

[72] J.-B. Uwineza, F. Rahman, F. Silva, W. Hu, and J. A. Farrell, "Characterizing GNSS Multipath at Different Antenna Mounting Positions on Vehicles," *UC Riverside: Bourns College of Engineering*, 2019. [Online]. Available: https://escholarship.org/uc/item/9mj3459s

[73] L.-T. Hsu, "GNSS Multipath Detection using a Machine Learning Approach," in *20th International Conf. on Intell. Transp. Syst.* IEEE, 2017, pp. 1–6.

[74] J. M. Mendel, *Lessons in Estimation Theory for Signal Processing, Communications, and Control*. Pearson Education, 1995.

[75] N. Sünderhauf and P. Protzel, "Towards a Robust Back-end for Pose Graph SLAM," *IEEE Robotics and Automation (ICRA)*, 2012.

[76] ——, "Switchable constraints for robust pose graph slam," *Intelligent Robots and Systems*, pp. 1879–1884, 2012.

[77] R. A. Fisher, "Statistical Methods for Research Workers," in *Breakthroughs in Statistics*. Springer, 1992, pp. 66–70.

[78] W. Hu, H. Mohsenian-Rad, and J. A. Farrell, "Optimization-Based Outlier Accommodation using Linear Performance Constraints for CAV State Estimation in Urban Environments," *under review*, 2024.

[79] W. Hu, J.-B. Uwineza, and J. A. Farrell, "Outlier Accommodation for GNSS Precise Point Positioning using Risk-Averse State Estimation," *arXiv preprint arXiv:2402.01860*.

[80] Z.-Q. Luo and P. Tseng, "On the Convergence of the Coordinate Descent Method for Convex Differentiable Minimization," *J. of Optimization Theory and Applications*, vol. 72, no. 1, pp. 7–35, 1992.

[81] D. P. Bertsekas, "Nonlinear Programming, 2nd edition edition," *Bertsekas, Athena Scientific, Belmont (Mass.)*, 1999.

[82] M. Dyer, B. Gärtner, N. Megiddo, and E. Welzl, "Linear Programming," in *Handbook of discrete and computational geometry*. Chapman and Hall/CRC, 2017, pp. 1291–1309.

[83] M. B. Cohen, Y. T. Lee, and Z. Song, "Solving Linear Programs in the Current Matrix Multiplication Time," *J. of the ACM (JACM)*, vol. 68, no. 1, pp. 1–39, 2021.

[84] T. Berthold, "Primal Heuristics for Mixed Integer Programs," Ph.D. dissertation, Zuse Institute Berlin (ZIB), 2006.

[85] E. L. Lawler and D. E. Wood, "Branch-and-Bound Methods: A Survey," *Operations research*, vol. 14, no. 4, pp. 699–719, 1966.

[86] A. Atamtürk, G. L. Nemhauser, and M. W. Savelsbergh, “Conflict Graphs in Solving Integer Programming Problems,” *European J. of Operational Research*, vol. 121, no. 1, pp. 40–55, 2000.

[87] E. Danna, E. Rothberg, and C. L. Pape, “Exploring Relaxation Induced Neighborhoods to Improve MIP Solutions,” *Mathematical Programming*, vol. 102, pp. 71–90, 2005.

[88] M. Grant and S. Boyd, “The CVX Users’ Guide, Release 2.2,” *CVX Research, Inc.*, 2020.

[89] M. Schmitz, “State space technology-principle, RTCM standardization and examples,” *GNSS-reference Networks. QUO VADIS, Hannover*, 2010.

[90] E. Aghapour and J. A. Farrell, “Outlier Accommodation in Moving-Horizon State Estimation: A Risk-Averse Performance-Specified Approach,” *International Journal of Adaptive Control and Signal Processing*, 2019.

[91] L. Narula, D. M. LaChapelle, M. J. Murrian, J. M. Wooten, T. E. Humphreys, J.-B. Lacambre, E. de Toldi, and G. Morvant, “TEX-CUP: The University of Texas Challenge for Urban Positioning,” in *Proceedings of the IEEE/ION PLANS Meeting*, Portland, OR, 2020.

Appendix A

Formulation of Linear Performance Specification Constraint

The purpose of this appendix is to reformulate the diagonal performance specification into a form that is a linear in the measurement selection variable.

The optimization problem of eqn. (5.3) has the constraint

$$\operatorname{diag}(\mathbf{J}_b^+) \geq \mathbf{J}_l \text{ where } \mathbf{J}_\mathbf{b}^+ = \sum_{i=1}^{m} \frac{b_i^2}{\sigma_i^2} \mathbf{h}_i^\top \mathbf{h}_i + \mathbf{J}^-, \tag{A.1}$$

where $\mathbf{J}_l$ is a positive semi-definite and diagonal matrix. This constraint can be manipulated as follows:

$$\begin{aligned}
\operatorname{diag}\left(\sum_{i=1}^{m} \frac{b_i^2}{\sigma_i^2} \mathbf{h}_i^\top \mathbf{h}_i + \mathbf{J}^-\right) &\geq \mathbf{J}_l \\
\operatorname{diag}\left(\sum_{i=1}^{m} \frac{b_i^2}{\sigma_i^2} \mathbf{h}_i^\top \mathbf{h}_i\right) &\geq \mathbf{J}_l - \mathbf{J}_d^- \\
\mathbf{G}\left(\mathbf{b} \circ \mathbf{b}\right) &\geq \mathbf{d}
\end{aligned} \tag{A.2}$$

where $\mathbf{J}_d^- = \operatorname{diag}(\mathbf{J}^-)$ and $\mathbf{b} \circ \mathbf{b}$ is the element-wise product (i.e., $\mathbf{b} \circ \mathbf{b} = [b_1^2, ..., b_m^2]^\top$), $\mathbf{d} = \mathbf{J}_l - \operatorname{diag}(\mathbf{J}^-)$ and

$$\mathbf{G} = \begin{bmatrix} \frac{h_{11}^2}{\sigma_1^2} & \frac{h_{21}^2}{\sigma_2^2} & \cdots & \frac{h_{m1}^2}{\sigma_m^2} \\ \frac{h_{12}^2}{\sigma_1^2} & \frac{h_{22}^2}{\sigma_2^2} & \cdots & \frac{h_{m2}^2}{\sigma_m^2} \\ \vdots & \vdots & \ddots & \vdots \\ \frac{h_{1n}^2}{\sigma_1^2} & \frac{h_{2n}^2}{\sigma_2^2} & \cdots & \frac{h_{mn}^2}{\sigma_m^2} \end{bmatrix}. \tag{A.3}$$

For the binary case, $b_i^2 = b_i$; therefore, the constraint can be represented as

$$\mathbf{G}\,\mathbf{b} \geq \mathbf{d}. \tag{A.4}$$

For the non-binary case, the optimization problem (5.3) is written as

$$\left.\begin{aligned} \hat{\mathbf{x}},\mathbf{b} = &\underset{\mathbf{x},\mathbf{b}}{\operatorname{argmin}}\ \|\mathbf{x}-\hat{\mathbf{x}}^{-}\|^2_{\mathbf{P}^{-}} + \sum_{i=1}^{m}\frac{b_i^2}{\sigma_i^2}(y_i-\mathbf{h}_i\mathbf{x})^2 \\ &\text{s.t.: } \mathbf{G}\left(\mathbf{b}\circ\mathbf{b}\right) \geq \mathbf{d} \\ &\quad b_i \in [0,\,1] \text{ for } i\,=\,1,\ldots m. \end{aligned}\right\} \tag{A.5}$$

Let $\nu_i = b_i^2 \in [0,1]$. Therefore, optimization problem (A.5) can be written as

$$\left.\begin{aligned} \hat{\mathbf{x}},\boldsymbol{\nu} = &\underset{\mathbf{x},\boldsymbol{\nu}}{\operatorname{argmin}}\ \|\mathbf{x}-\hat{\mathbf{x}}^{-}\|^2_{\mathbf{P}^{-}} + \sum_{i=1}^{m}\frac{\nu_i}{\sigma_i^2}(y_i-\mathbf{h}_i\mathbf{x})^2 \\ &\text{s.t.: } \mathbf{G}\boldsymbol{\nu} \geq \mathbf{d} \\ &\quad \nu_i \in [0,\,1] \text{ for } i\,=\,1,\ldots m. \end{aligned}\right\} \tag{A.6}$$

Optimization problem (A.6) is linear in $\boldsymbol{\nu}$. In the problem statement, the symbol $\boldsymbol{\nu}$ is a dummy variable. In the main body of the article (see Problem (5.5)), $\boldsymbol{\nu}$ will be replaced by $\mathbf{b}$.

Appendix B

Derivation from Continuous-time Model to Discrete-time Model

The purpose of this appendix is to derive the PVA discrete-time model from its continuous-time model.

The continuous-time state vector is defined as

$$\mathbf{x}(t) = [\mathbf{p}_r(t), \mathbf{v}_r(t), \mathbf{a}_r(t), \boldsymbol{\Delta}^{\gamma}(t), r_c(t)]^{\top} \in \Re^{n} \tag{B.1}$$

where $\mathbf{p}_r(t), \mathbf{v}_r(t), \mathbf{a}_r(t) \in \Re^{n}$, and $\boldsymbol{\Delta}^{\gamma}(t) \in \Re^{n_s}$.

The position, velocity, acceleration, and clock system continuous-time models are defined as

$$\dot{\mathbf{p}}_r(t) = \mathbf{v}_r(t), \;\; \dot{\mathbf{v}}_r(t) = \mathbf{a}_r(t), \;\; \dot{\mathbf{a}}_r(t) = \boldsymbol{\eta}_a(t), \;\; \dot{\Delta}_i^{\gamma}(t) = r_c(t), \;\; \dot{r}_c(t) = \eta_{\Delta}(t), \tag{B.2}$$

where $\boldsymbol{\eta}_a(t) = [\eta^2_{a_x}(t), \eta^2_{a_y}(t), \eta^2_{a_z}(t)]$ is a vector of continuous-time Gaussian white noise terms with Power Spectral Density (PSD) of $\boldsymbol{\sigma}^2_{a_x}$, $\boldsymbol{\sigma}^2_{a_y}$, and $\boldsymbol{\sigma}^2_{a_z}$, respectively, $\eta_\Delta(t)$ is the continuous-time Gaussian white noise with PSD of σ^2_Δ, and $\dot{\Delta}^\gamma_i(t)$ is the derivative of i-th element of $\boldsymbol{\Delta}^\gamma(t)$. Acceleration $\mathbf{a}_r$ and clock drift r_c are modeled as a random walk because they are updated frequently, with the measurement update step occurring every second.

Therefore, the continuous-time system is $\dot{\mathbf{x}}(t) = \mathscr{F}\,\mathbf{x}(t) + \mathbf{G}\,\boldsymbol{\eta}(t)$, where

$$\mathscr{F} = \begin{bmatrix} \mathbf{0} & \mathbf{I}_3 & \mathbf{0} & \mathbf{0} & \mathbf{0} \\ \mathbf{0} & \mathbf{0} & \mathbf{I}_3 & \mathbf{0} & \mathbf{0} \\ \mathbf{0} & \mathbf{0} & \mathbf{0} & \mathbf{0} & \mathbf{0} \\ \mathbf{0} & \mathbf{0} & \mathbf{0} & \mathbf{0} & \mathbf{T}_{n_s} \\ \mathbf{0} & \mathbf{0} & \mathbf{0} & \mathbf{0} & 0 \end{bmatrix}, \quad \mathbf{G} = \begin{bmatrix} \mathbf{0} & \mathbf{0} & \mathbf{0} & \mathbf{0} & \mathbf{0} \\ \mathbf{0} & \mathbf{0} & \mathbf{0} & \mathbf{0} & \mathbf{0} \\ \mathbf{0} & \mathbf{0} & \mathbf{I}_3 & \mathbf{0} & \mathbf{0} \\ \mathbf{0} & \mathbf{0} & \mathbf{0} & \mathbf{0} & \mathbf{0} \\ \mathbf{0} & \mathbf{0} & \mathbf{0} & \mathbf{0} & 1 \end{bmatrix}, \quad \boldsymbol{\eta}(t) = \begin{bmatrix} \mathbf{0} \\ \mathbf{0} \\ \eta_a(t) \\ \mathbf{0} \\ \eta_\Delta(t), \end{bmatrix} \tag{B.3}$$

and $\boldsymbol{\eta}(t) \sim \mathcal{N}(\mathbf{0}, \mathbf{Q})$ is the continuous-time process noise where $\mathbf{Q} = diag([\mathbf{0};\ \mathbf{0};\ \boldsymbol{\sigma}^2_a;\ \mathbf{0};\ \sigma^2_\Delta])$ where $\boldsymbol{\sigma}^2_a = [\boldsymbol{\sigma}^2_{a_x}; \boldsymbol{\sigma}^2_{a_y}; \boldsymbol{\sigma}^2_{a_z}]$. Other symbols are defined after eqn. (4.3).

The corresponding discrete-time state-space model is represented by

$$\begin{aligned} \mathbf{x}_{k+1} &= \mathbf{F}\,\mathbf{x}_k + \mathbf{w}_k, \\ \mathbf{P}_{k+1} &= \mathbf{F}\,\mathbf{P}_k\,\mathbf{F}^\top + \mathbf{Q}_d. \end{aligned}$$

where $\mathbf{P}_k$ is the error covariance matrix of state $\mathbf{x}_k$. Using the methods discussed in Section 4.7 of [8], the exact solution of $\mathbf{F}$ is derived by

$$\begin{aligned}
\mathbf{F}(\tau,t) &= \exp^{\mathscr{F}(\tau-t)} \\
\mathbf{F}(T) &= \exp^{\mathscr{F}T} \\
&= \mathbf{I}+\mathscr{F}T+\frac{1}{2}(\mathscr{F}T)^2+\cdots \\
&= \mathbf{I}+\mathscr{F}T+\frac{1}{2}(\mathscr{F}T)^2 \\
&= \begin{bmatrix}
\mathbf{I}_{3\times3} & T\,\mathbf{I}_{3\times3} & \frac{1}{2}T^2\,\mathbf{I}_{3\times3} & \mathbf{0} & \mathbf{0} \\
\mathbf{0} & \mathbf{I}_{3\times3} & T\,\mathbf{I}_{3\times3} & \mathbf{0} & \mathbf{0} \\
\mathbf{0} & \mathbf{0} & \mathbf{I}_{3\times3} & \mathbf{0} & \mathbf{0} \\
\mathbf{0} & \mathbf{0} & \mathbf{0} & \mathbf{I}_{n_s\times n_s} & \mathbf{T}_{n_s} \\
\mathbf{0} & \mathbf{0} & \mathbf{0} & \mathbf{0} & 1
\end{bmatrix},
\end{aligned} \tag{B.4}$$

where $T = t_{k+1} - t_k$. The exact solution of process noise matrix $\mathbf{Q}_d$ is derived by

$$
\begin{aligned}
\mathbf{Q}_d &= \int_{t_k}^{t_{k+1}} \mathbf{F}(t_{k+1}, s)\, \mathbf{G}\, \mathbf{Q}, \mathbf{G}^\top \mathbf{F}(t_{k+1}, s)^\top ds \\
&= \int_0^T \mathbf{F}(s)\, \mathbf{G}\, \mathbf{Q}\, \mathbf{G}^\top \mathbf{F}(s)^\top ds \\
&= \int_0^T \begin{bmatrix} \mathbf{0} & \mathbf{0} & \frac{1}{2}s^2 \mathbf{I}_{3\times3} & \mathbf{0} & \mathbf{0} \\ \mathbf{0} & \mathbf{0} & s\mathbf{I}_{3\times3} & \mathbf{0} & \mathbf{0} \\ \mathbf{0} & \mathbf{0} & \mathbf{I}_{3\times3} & \mathbf{0} & \mathbf{0} \\ \mathbf{0} & \mathbf{0} & \mathbf{0} & \mathbf{0} & \mathbf{T}_{n_s} \\ \mathbf{0} & \mathbf{0} & \mathbf{0} & \mathbf{0} & 1 \end{bmatrix} \mathbf{Q} \begin{bmatrix} \mathbf{0} & \mathbf{0} & \mathbf{0} & \mathbf{0} & \mathbf{0} \\ \mathbf{0} & \mathbf{0} & \mathbf{0} & \mathbf{0} & \mathbf{0} \\ \frac{1}{2}s^2 \mathbf{I}_{3\times3} & s\mathbf{I}_{3\times3} & \mathbf{I}_{3\times3} & \mathbf{0} & \mathbf{0} \\ \mathbf{0} & \mathbf{0} & \mathbf{0} & \mathbf{0} & \mathbf{0} \\ \mathbf{0} & \mathbf{0} & \mathbf{0} & \mathbf{T}_{n_s}^\top & 1 \end{bmatrix} ds \\
&= \begin{bmatrix} \frac{T^5}{20}\mathbf{Q}_a & \frac{T^4}{8}\mathbf{Q}_a & \frac{T^3}{6}\mathbf{Q}_a & \mathbf{0} & \mathbf{0} \\ \frac{T^4}{8}\mathbf{Q}_a & \frac{T^3}{3}\mathbf{Q}_a & \frac{T^2}{2}\mathbf{Q}_a & \mathbf{0} & \mathbf{0} \\ \frac{T^3}{6}\mathbf{Q}_a & \frac{T^2}{2}\mathbf{Q}_a & T\,\mathbf{Q}_a & \mathbf{0} & \mathbf{0} \\ \mathbf{0} & \mathbf{0} & \mathbf{0} & \frac{\sigma_\Delta^2}{3} T^3 \mathbf{\Lambda}_{n_s} & \frac{\sigma_\Delta^2}{2} T^2 \mathbf{T}_{n_s} \\ \mathbf{0} & \mathbf{0} & \mathbf{0} & \frac{\sigma_\Delta^2}{2} T^2 \mathbf{T}_{n_s}^\top & T \end{bmatrix}
\end{aligned}
\tag{B.5}
$$

where $\mathbf{\Lambda}_{n_s}$ is a n_s by n_s matrix with all elements equal to one.

Appendix C

Convex Problem Formulation of Binary DiagRAPS

This appendix is to derive the convex optimization form of DiagRAPS for binary measurement selection variables **b**. The DiagRAPS optimization problem of eqn. (5.4) for binary vector **b** is written as

$$\left.\begin{aligned} \hat{\mathbf{x}}, \mathbf{b} =& \underset{\mathbf{x},\mathbf{b}}{\operatorname{argmin}} \, \|\mathbf{x}-\hat{\mathbf{x}}^{-}\|^2_{\mathbf{P}^{-}} + \sum_{i=1}^{m} \frac{b_i^2}{\sigma_i^2}(y_i - \mathbf{h}_i\mathbf{x})^2 \\ & \text{s.t.: } \mathbf{G}\,\mathbf{b} \geq \mathbf{d}, \\ & \quad b_i \in \{0,\, 1\} \text{ for } i = 1, \ldots m. \end{aligned}\right\} \tag{C.1}$$

where $b_i^2 = b_i$ is the nature of binary variables. Therefore, Problem (C.1) can be represented as

$$\left.\begin{aligned} \hat{\mathbf{x}}, \mathbf{b} =& \underset{\mathbf{x},\mathbf{b}}{\operatorname{argmin}} \, \|\mathbf{x}-\hat{\mathbf{x}}^{-}\|^2_{\mathbf{P}^{-}} + \sum_{i=1}^{m} \frac{(y_i b_i - \mathbf{h}_i b_i \mathbf{x})^2}{\sigma_i^2} \\ & \text{s.t.: } \mathbf{G}\,\mathbf{b} \geq \mathbf{d}, \\ & \quad b_i \in \{0,\, 1\} \text{ for } i = 1, \ldots m. \end{aligned}\right\} \tag{C.2}$$

Introduce a new vector $\mathbf{q} = [\mathbf{q}_1; ...; \mathbf{q}_i; ...; \mathbf{q}_m] \in \mathbb{R}^{n\times m}$ where $\mathbf{q}_i = b_i\mathbf{x} = [q_{i1}, ..., q_{ij}, ..., q_{in}]^\top \in \mathbb{R}^n$ where $q_{ij} = b_i x_j$ where x_j is j-th element of $\mathbf{x}$. While the multiplication $b_i x_i$ is non-convex, non-linear, and mixed-binary, the new variable can be constrained by linear constraints as

$$\mathbf{x}_{min} \leq \mathbf{x} \leq \mathbf{x}_{max}, \tag{C.3}$$

$$\mathbf{x} - \mathbf{x}_{max}(1 - b_i) \leq \mathbf{q}_i \leq b_i\mathbf{x}_{max}, \tag{C.4}$$

$$b_i\mathbf{x}_{min} \leq \mathbf{q}_i \leq \mathbf{x} - \mathbf{x}_{min}(1 - b_i), \tag{C.5}$$

where $\mathbf{x}_{min}$ and $\mathbf{x}_{max}$ are the lower bound and upper bound of $\mathbf{x}$. respectively. For a state estimation problem, these bounds can be set to $\hat{\mathbf{x}}^- \pm \mathbf{\Delta}$ where $\mathbf{\Delta}$ can be a large positive value of engineering bound. The linear constraints in eqn. (C.4) and eqn. (C.5) construct interesting features for $\mathbf{q}$.

1. When $b_i = 1$, eqn. (C.4) is $\mathbf{x} \leq \mathbf{q}_i \leq \mathbf{x}_{max}$ and eqn. (C.5) is $\mathbf{x}_{min} \leq \mathbf{q}_i \leq \mathbf{x}$, which ensure that $\mathbf{q}_i = \mathbf{x}$;

2. When $b_i = 0$, eqn. (C.4) is $\mathbf{x} - \mathbf{x}_{max} \leq \mathbf{q}_i \leq 0$ and eqn. (C.5) is $0 \leq \mathbf{q}_i \leq \mathbf{x} - \mathbf{x}_{min}$, which ensure that $\mathbf{q}_i = \mathbf{0}$.

The linear constraints therefore guarantee that the new variables q_{ij} is consistent with its definition of $b_i x_j$. In consequence, for binary vector $\mathbf{b}$, the convex objective function is written as

$$C_c(\mathbf{x}, \mathbf{b}, \mathbf{q}) = \|\mathbf{x} - \hat{\mathbf{x}}^-\|^2_{\mathbf{P}^-} + \sum_{i=1}^{m} \frac{(y_i b_i - \mathbf{h}_i\mathbf{q}_i)^2}{\sigma_i^2},$$

and the convex DiagRAPS optimization problem can be formulated by

$$\left.\begin{aligned}
\hat{\mathbf{x}},\mathbf{b},\mathbf{q} =&\underset{\mathbf{x},\mathbf{b},\mathbf{q}}{\text{argmin}}\, C_c(\mathbf{x},\mathbf{b},\mathbf{q}) \\
&\text{s.t.: } \mathbf{G}\,\mathbf{b} \geq \mathbf{d}, \\
&\quad b_i \in \{0,\, 1\} \text{ for } i = 1, \ldots m, \\
&\quad \mathbf{x}_{min} \leq \mathbf{x} \leq \mathbf{x}_{max}, \\
&\quad \mathbf{x} - \mathbf{x}_{max}(1-b_i) \leq \mathbf{q}_i \leq b_i\,\mathbf{x}_{max}, \\
&\quad b_i\,\mathbf{x}_{min} \leq \mathbf{q}_i \leq \mathbf{x} - \mathbf{x}_{min}(1-b_i).
\end{aligned}\right\} \tag{C.6}$$

Problem (C.6) has a non-linear convex objective function and linear constraints. It is equivalent to the original DiagRAPS optimization problem. However, it is mixed-integer non-linear convex optimization problem. Compare to the non-convex form, this new form introduces additional $n \times m$ variables.

When the soft constraint is applied as discussed in Sec. 6.5. The convex objective function is formulated by

$$C_g(\mathbf{x},\mathbf{b},\mathbf{q},\boldsymbol{\mu}) = \|\mathbf{x}-\hat{\mathbf{x}}^-\|^2_{\mathbf{P}^-} + \sum_{i=1}^{m} \frac{(y_i\,b_i - \mathbf{h}_i\,\mathbf{q}_i)^2}{\sigma_i^2} + \lambda \sum_{j=1}^{n} \boldsymbol{\mu}, \tag{C.7}$$

and the relaxed convex DiagRAPS optimization problem is written as

$$\left.\begin{aligned}
&\hat{\mathbf{x}}, \mathbf{b}, \mathbf{q}, \boldsymbol{\mu} = \underset{\mathbf{x}, \mathbf{b}, \mathbf{q}, \boldsymbol{\mu}}{\operatorname{argmin}} \, C_g(\mathbf{x}, \mathbf{b}, \mathbf{q}, \boldsymbol{\mu}) \\
&\qquad \text{s.t.: } \mathbf{g}_j \mathbf{b} + \mu_j \geq d_j - L_j, \\
&\qquad\quad \mu_j \in \begin{cases} [0, L_j], & \mathbf{g}_j \mathbf{1} > d_j \\ [0, \mathbf{g}_j \mathbf{1}], & \mathbf{g}_j \mathbf{1} \leq d_j \end{cases} \text{ for } j = 1, \ldots n, \\
&\qquad\quad b_i \in \{0, 1\} \text{ for } i = 1, \ldots m, \\
&\qquad\quad \mathbf{x}_{min} \leq \mathbf{x} \leq \mathbf{x}_{max}, \\
&\qquad\quad \mathbf{x} - \mathbf{x}_{max}(1 - b_i) \leq \mathbf{q}_i \leq b_i \mathbf{x}_{max}, \\
&\qquad\quad b_i \mathbf{x}_{min} \leq \mathbf{q}_i \leq \mathbf{x} - \mathbf{x}_{min}(1 - b_i).
\end{aligned}\right\} \tag{C.8}$$